The People's Democratic Republic of Algeria Ministry of Higher Education and Scientific Research

Dr. Yahia Fares University, Medea
Faculty of Technology

Master dissertation
In Electrical engineering
Specialization: Renewable Energy

Entitled

Performance Enhancement of Solar Water Pumping Systems Using Deep Learning

Presented by:
ZEROUAK Noureddine

Under the guidance and supervision of
Pr. HAMIDIA. Fethia
Ms. BOUKIRATE. Samia

June 2025

Acknowledgments

*First and foremost, I would like to thank **Allah** for granting me the courage, patience, and strength to carry out this work throughout my years of study.*

*I express my deepest gratitude to my professors, **Dr. F. Hamidia** and **Ms. S. Boukirate**, for their constant availability, valuable guidance, insightful advice, and exceptional kindness.*

*I also extend my sincere appreciation to the committee members, **Dr. Y. Tami** and **Dr. Khalif**, for devoting their time and for kindly accepting to examine and evaluate this modest work.*

*My heartfelt thanks go to all the **teachers of the Electrical Engineering Department** for their continuous support and the knowledge they have shared with me throughout my academic journey.*

Finally, I would like to sincerely thank everyone who supported me, whether directly or indirectly, and all those who generously gave me their time and encouragement.

Dedication

I dedicate this work:

*To my beloved **Parents**, for their unconditional love, endless support, and constant encouragement. Your sacrifices, prayers, and guidance have been the foundation of my journey.*

*To my **families**, who have always stood by my side and believed in me through every challenge.*

*To my **friends**, whose presence, motivation, and companionship made this journey more meaningful and enjoyable.*

And finally, to all those who inspired and supported me, directly or indirectly, throughout this experience this achievement is as much yours as it is mine.

ملخص:

تُستخدم الطاقة الشمسية بشكل واسع في أنظمة الضخ بالمياه، وتُظهر خصائص الألواح الكهروضوئية تحت تأثير التظليل الجزئي عدة نقاط قدرة محلية، مما يجعل من الصعب على الطرق التقليدية تتبع النقطة العالمية المثلى ويؤدي إلى خسارة في الطاقة. في هذا العمل، تم اقتراح استخدام الذكاء الاصطناعي، عبر الشبكات العصبية العميقة (**DNN**) والسطحية (**SNN**) ، لتحسين تقنية تتبع نقطة القدرة القصوى(**MPPT**) ، من أجل رفع كفاءة نظام الضخ الكهروضوئي. تم التحكم في آلة غير متزامنة باستخدام تقنية التحكم المباشر في العزم (**DTC**) أظهرت نتائج المحاكاة فعالية النظام المقترح في ظروف الإشعاع المثالية وكذلك عند التظليل، مع أداء متميز في تتبع نقطة القدرة القصوى، تقليل التذبذبات، وتحسين استقرار النظام.

الكلمات المفتاحية :
النظام الكهروضوئي:**PV SYSTEM** ، تقنية تتبع نقطة القدرة القصوى: **MPPT** ، الشبكات العصبية العميقة: **DNN** والسطحية **SNN**، آلة غير متزامنة : **IM** ، التحكم المباشر في العزم: **DTC** ، تظليل جزئي: **PS**.

Abstract :

Photovoltaic energy is widely used in water pumping systems. Under partial shading, the **PV** power-voltage curve exhibits multiple local maxima, making it difficult for traditional **MPPT** algorithms to reach the global maximum power point (**GMPP**), resulting in energy losses.

In this work, we propose the use of artificial intelligence, specifically, Deep Neural Networks (**DNN**) and Shallow Neural Networks (**SNN**) to enhance **MPPT** techniques and improve the overall performance of a **PV** pumping system. The induction machine is controlled via Direct Torque Control (**DTC**). Simulation results confirmed the efficiency of the proposed system in both ideal and shaded conditions, with improved tracking, reduced oscillations, and enhanced stability.

Keywords: PV system, MPPT, DNN, SNN, Induction Machine, DTC, Partial Shading.

Résumé

L’énergie photovoltaïque est largement utilisée dans les systèmes de pompage d’eau. En cas d’ombrage partiel, la courbe puissance-tension du panneau **PV** présente plusieurs maxima locaux, rendant difficile pour les techniques classiques d’atteindre le point de puissance maximale global (**GMPP**), ce qui entraîne des pertes d’énergie.

Ce travail propose l’utilisation de l’intelligence artificielle, à travers les réseaux de neurones profonds (**DNN**) et superficiels (**SNN**), pour améliorer le suivi du point de puissance maximale (**MPPT**) et optimiser le rendement d’un système de pompage photovoltaïque. La machine asynchrone est commandée par la technique de contrôle direct du couple (**DTC**). Les résultats de simulation ont démontré l’efficacité du système proposé dans des conditions idéales et en présence d’ombrage, avec de meilleures performances de suivi, moins d’oscillations, et une stabilité améliorée.

Mots-clés : **système PV, MPPT, DNN, SNN, machine asynchrone, DTC, ombrage partiel.**

TABLE OF CONTENTS

General Introduction..... 1

Chapter I: Photovoltaic (PV) System

I.1 Introduction..... 3
I.2 Photovoltaic System..... 3
I.2.1 Definition..... 3
I.2.2 Operating principle..... 3
I.3 Photovoltaic cell..... 4
I.3.1 The different types of solar cells…..... 5
I.3.2 Efficiency…….....6
I.3.3 Electrical characteristics of a photovoltaic cell..... 7
I.3.4 Parameters of a photovoltaic cell 8
I.3.4.1 Short-circuit current 8
I.3.4.2 Open circuit voltage 8
I.3.4.3 Energy efficiency 9
I.3.4.4 Fill factor..... 9
I.3.4.5 Maximum power point (P_{mpp}) 9
I.4 Photovoltaic generator and its performance 10
I.4.1 Influence of the series association of PV cells.....10
I.4.2 Influence of parallel association of PV cells..... 10
I.4.3 Influence of mixed association (Series + parallel) of PV cells…… 11
I.5 Photovoltaic panel 11
I.6 Photovoltaic (PV) System Simulation 12
I.6.1 Current-Voltage characteristic 12
I.6.2 Power-voltage characteristic 13
I.6.3 Influence of illumination and temperature on the curves I=f (V) and P=f (V)…… 14
I.6.4 Series-parallel association 15
I.6.5 Analysis of power curves (P-V and I-V) 16
I.7. Protection of Photovoltaic system..... 16
I.7.1 Overcurrent protection…….....17
I.7.2 Overvoltage Protection…… 17
I.7.3 Ground Fault protection…..... 17
I.7.4 Isolation and Switching…….....17
I.7.5 Protection against Electric Shock…… 17
I.7.6 Fire Protection…….....17
I.7.7 Environmental Protection…….....18
I.8. Shading…….....18
I.8.1 Definition of Shading in PV systems…….....18
I.8.2 Effects of Shading on PV system…….....19

I.9. Advantages and Drawbacks of Photovoltaic Energy ……..... 19
I.9.1 Advantages…….…….... 19
I.9.2 Drawbacks……... 19
I.10 Conclusion……... 20

Chapter II: DC-DC Converters

II.1 Introduction..... 21
II.2 DC-DC Converters (Choppers) 21
II.2.1 Modeling of the Boost Converter..... 21
II.2.2 Modeling of the Buck Converter (Step-down) 24
II.2.2 Modeling of the Buck-boost Converter……..... 27
II.3 MPPT-Control …….... 29
II.3.1 MPPT Control Classification…….... 29
II.3.2 Indirect MMPT Methods 29
II.3.3 Direct MPPT Methods 30
II.4 Conclusion 30

Chapter III: Modeling of Induction machine

III.1Introduction 32
III.2 General Information 32
III.2.1 Definition .....
32
III.2.2 Composition of the asynchronous machine: 32
III.2.2.1 Stator 33
III.2.2.2 Rotor 34
III.3 Representation of the three-phase asynchronous machine in electrical space…….35
III.4 Modeling of the asynchronous machine 37
III.4.1 Simplifying assumptions 37
III.4.2 Equations of the Generalized Asynchronous machine 37
III.4.3 Electrical equations 38
III.4.4 Magnetic equation..... 39
III.4.5 Mechanical equation 40
III.5 Three-phase/biphase transformations 41
III.5.1 Clarke transformation 41
III.5.2 Concordia transformation……..... 41
III.5.3 Park transformation 42
III.5.4 Application of Park transformation 44
III.5.5 Choice of reference system 44

III.6 Model of the asynchronous machine in the (d, q) frame of reference:..... 45
III.7 Modeling of the voltage inverter..... 45
III.7.1 Voltages in the phases of the induction machine..... 46
III.8 Simulation Results and Analysis..... 47
III.9 Conclusion 49

Chapter IV: Direct Torque Control of Induction machine

IV.1 Introduction.....50
IV.2 The principle of direct torque control..... 50
IV.2.1 Operation of a Three-Phase Voltage Inverter 51
IV.2.2 Stator flux and electromagnetic torque control..... 53
IV.2.2.1 Stator flux control 53
IV.2.2.2 Electromagnetic torque control 55
IV.2.3 Choice of the voltage Vector 56
IV.3 Estimators..... 58
IV.5.1 Estimation of the stator flux..... 58
IV.5.2 Estimation of the electromechanical torque 59
IV.4 Development of the control vector 59
IV.4.1 Flux controller 59
IV.4.2 Electromagnetic torque controller 60
IV.4.2.1 Two-level correctors 60
IV.4.2.2 Three-level correctors 60
IV.4.3 Development of switching table..... 61
IV.5 Simulation results for DTC of IM..... 62
IV.6 Conclusion 63

Chapter V: PV Pumping System Based on MPPT - Deep Learning

V.1 Introduction..... 65
V.2 Artificial Intelligence (AI) overview..... 65
V.3 Machine Learning Techniques 66
V.3.1. Types of Machine Learning Techniques 66
V.3.2. Supervised Learning……..... 66
V.3.3. Unsupervised Learning……..... 67
V.3.4. Reinforcement Learning……..... 67
V.4. Deep Learning Overview 68
V.4.1. Definition and Principles …..... 68
V.4.2. Multi-Layer Perceptron (MLP) 68
V.4.3. Convolutional Neural Networks (CNNs) 69
V.4.4. Recurrent Neural Networks (RNNs) 69

V.4.5. Deep Reinforcement Learning: 69
V.5 Artificial Neural Network 70
V.5.1 Neuron Input Computation 71
V.5.2 Activation Function 71
V.5.3 Output Computation..... 71
V.6 Architectures of MLP Neural Network..... 72
V.6.1 Shallow Neural Network (SNN)..... 72
V.6.2 Deep Neural Network..... 72
V.7 Artificial Neural Network based MPPT for Solar System..... 72
V.7.1 Training procedure 73
V.7.2 ANN-MPPT Algorithm with DC load under irradiation variation 74
V.7.3 DNN-MPPT Algorithm with DC load Partial Shading Condition 77
V.7.4 Proposed-MPPT Algorithm with AC load (Pumping System) 79
V.8 Conclusion 80

General conclusion..... 81

List of Figures

Chapter I: Photovoltaic (PV) System

Figure (I.1): The operating principle of a Solar cell……..……...04
Figure (I.2): Basic structure of a Solar cell ……..……...05
Figure (I.3): Equivalent electrical diagram of the photovoltaic cell……...…07
Figure (I.4): Mismatch for cells connected in series ……..……10
Figure (I.5): Mismatch for cells connected in parallel ……..……11
Figure (I.6): Modules protected by by-pass blocking diodes…….……12
Figure (I.7): Characteristic I =f (V) of a photovoltaic module …….…….13
Figure (I-8): Power-Voltage Characteristic of PV module P=f (V)…….…...14
Figure (I.9): The influence of illumination on the characteristic I=f(V)……..…...14
Figure (I.10): The influence of temperature on the characteristic I=f(V)……..15
Figure (I-11): Series-parallel association of PV cell……..….....16
Figure (I-12): Impact of partial shading on the P (V) characteristic……18

Chapter II: DC-DC Converter

Figure (II.1): Electrical schematic of the boost converter ……..…….22
Figure (II.2): Equivalent schematics of the boost chopper,……..…..... 22
Figure (II.3): Voltage and current characteristics of the boost converter……..…. 22
Figure (II.4): Electrical schematic of the Buck converter…….....……24
Figure (II.5): Equivalent schematics of the Buck chopper……...24
Figure (II.6): Voltage and current characteristics of the buck converter …….....…26
Figure (II.7): Variation of the load voltage with the load current for a Buck Converter…….26
Figure (II.8): Electrical diagram of a buck-boost converter……..……..27
Figure (II.9): Equivalent schematics of the Buck-boost chopper……..……..27
Figure (II.10): Voltage and current characteristics of the buck-boost converter…….....28
Figure (II.11): Principle of MPPT control……..….29

Chapter III: Modeling of Induction machine

Figure (III.1): Asynchronous (induction) motor……..……....…….33
Figure (III.2): Stator of the asynchronous machine…….……....…….33
Figure (III.3): Squirrel-cage rotor…….…….……..34
Figure (III.4): Magnetic circuit……..……..34
Figure (III.5): Wound rotor…….…….....35
Figure (III.6): Representation of the three-phase asynchronous machine in electrical space.….36
Figure (III.7): Transformation from Three-Phase (abc) to Concordia ($\alpha\beta$) Frame…….....42
Figure (III.8): Diagram of the IM in Park's reference frame……..…….……..…... 43
Figure (III.9): Representation of the two-level inverter feeding an IM…….……46

Figure (III.10): Simulation results of an induction machine without PWM……....48
Figure (III.11): Simulation results of an induction machine with PWM…….....48

Chapter IV: Direct Torque Control of Induction machine

Figure (IV.1): General block diagram of DTC controlled Induction motor ….…….... 51
Figure (IV.2): Asynchronous Machine Controlled by a Voltage Inverter…….……...52
Figure (IV.3): Operating Sequences of a Two-Level Voltage Inverter…….……53
Figure (IV.4): Evolution of the end of vector ϕ_s for negligible $R_s.I_s$ .....….54
Figure (IV.5): Choice of voltage vector…..…….……57
Figure (IV.6): No significant change…….…..…..…...…...57
Figure (IV.7): Hysteresis flux corrector……..……..59
Figure (IV.8): Three level torque corrector……..……..61
Figure (IV.9): Evolution of torque, stator flux and IM-DTC current……..63

Chapter V: PV Pumping System Based on MPPT - Deep Learning

Figure (V.1): Diagram of AI……...……...……...65
Figure (V-2): Machine Learning Techniques……..……..……...……65
Figure (V-3): Supervised Learning……...……..…….67
Figure (V-4): Unsupervised Learning……..……..…….67
Figure (V-5): Reinforcement Learning……..……..….68
Figure (V-6): Multi-Layer Perceptron……..…….....….69
Figure (V-7): Convolutional Neural Networks……..…….. ……..69
Figure (V-8): Recurrent Neural Networks…….……..……..……..70
Figure (V-9): Deep Reinforcement Learning……...……..…..……70
Figure (V-10): Comparison Between Biological Neuron and Artificial Neuron……71
Figure (V-11): Schematic of shallow neural network……..……...….72
Figure (V-12): Schematic of Deep neural network…….....…...….72
Figure (V.13): Training Procedure of ANN based MPPT for Solar PV System…….....…..74
Figure (V-14): Temporal Variation of Solar Irradiance …….……75
Figure (V-15): Performance Comparison of Deep and Shallow Neural Network-Based MPPT Under (PSC)……..76
Figure (V-16) PV-DC Load and (P-V) curve under partial shading…….……..77
Figure (V-17): Performance Evaluation of Deep Neural Network-Based MPPT Under Partial Shading Conditions …….....……..…78
Figure (V-18): The proposed system…….…...79
Figure (V-19): Training Performance of Deep Neural Network for MPPT Under Partial Shading – Case Study 2……...……80
Figure (V.20): System Performance under MPPT Control Without Shading……..……80
Figure (V.21): System Performance under MPPT Control With Partial Shading……....81

List of Tables

Chapter I

Table (I-1): Efficiency of different types of photovoltaic cells……...……..…06

Chapter IV

Table (IV.1): Different strategies of switching tables…….…….....61
Table (IV.5): Control strategy with a two-level hysteresis comparator…….……..62

NOTATION AND ABREVIATION

Chapter I – Photovoltaic System Notations

I	: The current supplied by the cell when operating as a generator (A).
V	: The terminal voltage of the same cell (V).
I_s	: Saturation current (A).
I_{ph}	: The photocurrent of the cell depends (A).
R_{se}	: Series resistance (Ω) of the photovoltaic cell.
R_{sh}	: The shunt resistance (Ω) of the photovoltaic cell.
K	: Boltzmann's constant (1.3819×10^{-23} J/K).
T	: The effective cell temperature in Kelvin (K).
q	: The electron charge ($q = 1.6 \times 10^{-19}$ C).
n	: The ideality factor of the junction ($1 < n < 2$).
I_{sc}	: The short circuit current (A).
V_{oc}	: The open circuit voltage (V).
p_{mpp}	: The maximum power (W).
V_{mpp}	: Maximum voltage (V).
I_{mpp}	: Maximum current (A).
FF	: The fill factor.
η	: The efficiency.
p_L	: Power of the incident light on the cell.
N_s	: Number of series cells.
N_p	: Number of parallel cells.

Chapter II – Converter Symbols

α	: The duty cycle.
T_s	: The impulse period.
L	: The inductor of the DC-DC converter.
K	: The switch of the DC-DC converter.
D	: The diode of the DC-DC converter.
C_1, C_2	: The two capacitors of the DC-DC converter.
V_{in}	: The input voltage on the DC-DC converter.
V_{out}	: The output voltage on the DC-DC converter.
I_{in}	: The input current on the DC-DC converter.
I_{out}	: The output current on the DC-DC converter.

Chapter III & IV – Induction Machine and DTC Symbols

ω_s	: The stator pulsation (rad/sec).
ω_r	: The rotor pulsation (rad/sec).
P_n	: The number of pole pairs.
Ω_s	: Slip speed.
V_{sa}, V_{sb}, V_{sc}	: Simple stator voltages (V).
V_{ra}, V_{rb}, V_{rc}	: Simple rotor voltages (V).
φ_s	: The stator flux (Wb).
φ_r	: The rotor flux (Wb).
R_s	: Stator resistance (Ω).
R_r	: Rotor resistance (Ω).
I_s	: Stator current (A).

I_r	: Rotor current (A).
L_s, L_r	: Stator and rotor inductance matrices (H).
L_m, L_{mr}	: Mutual inductance matrices between stator and rotor (H).
l_s, l_r	: Stator and rotor inductance coefficients (H).
m_s, m_r	: Maximum values of mutual inductance between stator and rotor (H).
T_{em}	: Electromagnetic torque (N·m).
T_r	: Resistive torque (N·m).
J	: The moment of inertia of the rotating parts (Kg·m²).
f	: Coefficient of friction (N·m·s/rad).
$P(\theta)$	: Park's transformation matrix.
V_{sdq0}, V_{rdq0}	: Stator and rotor voltages in the (d, q, 0) frame.
I_{sdq0}, I_{rdq0}	: Stator and rotor currents in the (d, q, 0) frame.
L_{s0}, L_{r0}	: Coefficient of stator and rotor zero-sequence inductance.
P_{elec}	: Electrical power (W).
θ_s	: Stator position (rad).
θ_r	: Rotor position (rad).
d	: Direct axis index.
q	: Quadrature axis index.
o	: Homopolar axis index.
σ	: Coefficient of magnetic dispersion.

Chapter V – General Abbreviations

GPV	: Photovoltaic generator
$MPPT$	: Maximum Power Point Tracking
AC	: Alternating current
DC	: Direct current
IM	: Induction machine
PWM	: Pulse Width Modulation
$GMPP$	: Global Maximum Power Point
$LMPP$	: Local Maximum Power Point
DNN	: Deep Neural Network
ANN	: Artificial Neural Network
SNN	: Shallow Neural Network
MLP	: Multi-Layer Perceptron
PSC	: Partial Shading Condition

General Introduction

General Introduction:

Energy production remains one of the greatest challenges of our century. As global electricity demand continues to rise, especially in emerging and developing regions, there is a pressing need for sustainable and reliable energy solutions. Among renewable sources, solar energy stands out for its abundance, availability, and capacity to meet off-grid demands in an environmentally friendly way. It represents a key pillar in the transition toward a cleaner, more sustainable and climate-resilient future. [1]

Photovoltaic (PV) systems, particularly in the field of solar-powered water pumping, have gained widespread attention. Since the late 1970s, PV pumping systems have become one of the most important real world applications of solar energy especially in rural and isolated areas where access to the electrical grid is economically unfeasible. These systems are not only clean and autonomous but also offer long-term cost-effectiveness [2]

To interface PV systems with mechanical components for tasks like water pumping**,** Induction Machines (IM) are often employed due to their robustness, low maintenance, and capability to operate under variable speed. However, for improved performance, advanced control techniques are necessary. Direct Torque Control (DTC) was developed to enhance the control of such machines in variable and renewable energy contexts, offering natural decoupling of flux and torque, faster dynamic response, and the elimination of the need for traditional PWM modulation blocks. Unlike conventional methods, DTC selects optimal inverter switching states directly based on torque and flux errors.

Another critical challenge in PV systems is the Maximum Power Point Tracking (MPPT) under varying irradiance and partial shading conditions. Shading can cause the appearance of multiple local peaks (LMPPs) and a single global maximum power point (GMPP), making traditional MPPT methods such as P&O and INC less effective. To overcome this, intelligent methods especially those based on Artificial Neural Networks (ANN) and Deep Learning (DNN**)** have been introduced. These data-driven algorithms offer adaptability, non-linear mapping capabilities, and faster convergence to the true global maximum point.

The main contribution of this thesis is to develop and validate a deep learning-based MPPT algorithm integrated with DTC control of an induction motor, applied to a PV-driven water pumping system. Simulation results prove the effectiveness of this combination in enhancing energy extraction, improving dynamic performance, and ensuring system reliability under different weather conditions.

This thesis is organized into five chapters:

The first chapter provides a general overview of photovoltaic systems. It discusses the working principle of PV cells, their electrical characteristics, and modeling techniques used to simulate their behavior under irradiance variation and partial shading conditions using MATLAB-Simulink.

The second chapter explores the role of DC-DC Converters in PV systems. It describes their basic operation, especially the Boost converter, and introduces traditional and AI-based MPPT algorithms that maximize the energy harvested from PV panels.

The third chapter deals with the mathematical modeling of the asynchronous machine using the d-q reference frame and explains how it interacts with voltage inverters using PWM. The chapter also covers the impact of control strategies on dynamic and steady-state motor performance.

The fourth chapter is dedicated to Direct Torque Control (DTC), highlighting its advantages in motor drive systems. It explains how DTC achieves flux and torque control without the need for PWM modulation, making it a robust method for controlling induction motors in PV-driven pumping systems.

The fifth and final chapter presents the proposed intelligent MPPT technique using a deep learning-based approach. The chapter validates the effectiveness of the hybrid DNN-MPPT and DTC scheme through detailed simulation results. Performance metrics such as tracking speed, torque ripple, and system efficiency are analyzed under various irradiation and shading conditions.

This thesis concludes with a comprehensive discussion of the results and demonstrates the advantages of combining deep learning and advanced motor control for improved renewable energy system performance. The proposed system proves to be a reliable and efficient solution for real world photovoltaic water pumping applications.

CHAPTER I:

Overview

Of PV Systems

I.1 Introduction:

A photovoltaic (PV) system is an electrical power system designed to convert solar energy into usable electrical energy. It mainly consists of a photovoltaic generator composed of one or more solar panels, a battery bank for energy storage, DC-DC converters to regulate voltage levels for batteries and DC loads, and a DC-AC inverter to supply AC-powered devices.

This chapter provides a comprehensive overview of photovoltaic systems. It begins with an introduction to photovoltaic technology, covering its definition, the basic operating principle, and the various types of photovoltaic cells along with their respective efficiencies. It then examines the electrical characteristics of PV cells, key parameters affecting their performance, and the impact of connecting modules in series and parallel configurations.

Furthermore, the chapter analyzes the power-voltage (P–V) and current-voltage (I–V) characteristics of PV modules under varying conditions of solar irradiance, cell temperature, and partial shading (PSC), supported by MATLAB simulation results. The chapter concludes by summarizing the key findings and insights discussed.

I.2. Photovoltaic System:

I.2.1. Definition:

The term "photovoltaic" comes from the Greek word meaning light, and is composed of two parts: "photos" "light" and the surname of the Italian physicist (Alessandro Volta) who invented the electric battery in 1800 and gave his name to the unit of measurement for electrical voltage, the volt [1].

I.2.2. Operating principle:

Figure (I.1) illustrates the internal structure and basic operating mechanism of a photovoltaic (PV) cell. When solar irradiance (G) strikes the surface, photons penetrate the cell and reach the P-N junction. This junction is formed by the contact between an N-doped (negatively charged) and a P-doped (positively charged) semiconductor region.

The energy from the photons excites electrons in the semiconductor material, creating electron-hole pairs. Due to the internal electric field at the P-N junction, electrons are driven toward the N-side and holes toward the P-side, creating a directional flow of current. This movement of charge carriers generates a voltage across the terminals (V_{cell}) and a current (I_{cell}) through an external circuit.

The front contact (metal grid) allows light to enter while conducting electricity and the back contact completes the circuit. Together, these layers enable the conversion of solar energy into electrical energy efficiently.

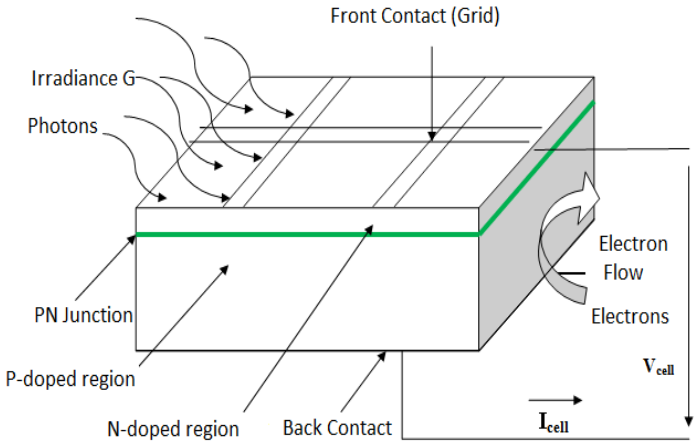


Figure (I.1): The operating principle of a solar cell [2].

I.3. Photovoltaic cell:

The PV cell, or solar cell, is the smallest component of a photovoltaic system. It is composed of semiconductor materials and directly converts light energy into electrical energy. Photovoltaic cells consist of:

- A thin semiconductor layer (a material with a band gap, which acts as an energy barrier that electrons cannot cross without external excitation, and whose electronic properties can be varied) such as silicon, which is a material with relatively good electrical conductivity.
- An anti-reflective layer allowing maximum penetration of solar rays.
- A conductive grid on top, or cathode, and a conductive metal on the bottom, or anode.
- The most recent ones even feature a new combination of reflective multilayers just below the semiconductor, allowing light to bounce around for longer periods of time to improve efficiency. [1]

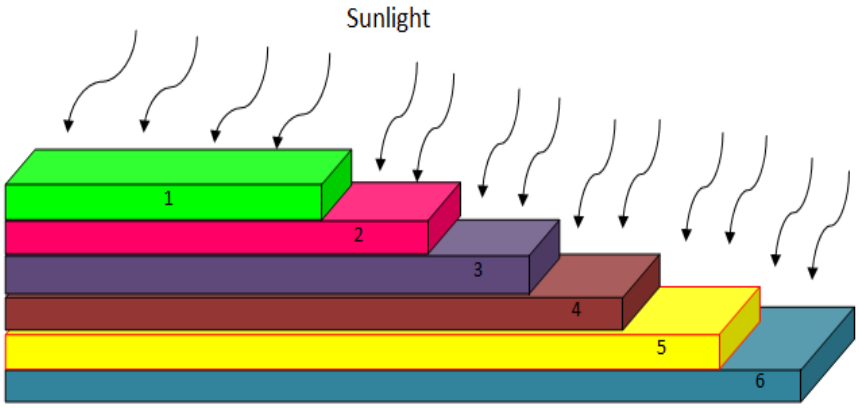


Figure (I.2): Basic structure of a solar cell [1].

1. Glass
2. Anti-reflection coating
3. Conductive grid
4. N-doped semiconductor
5. P-doped semiconductor
6. Conductors

A photovoltaic cell is based on the physical phenomenon called the photovoltaic effect which consists of establishing an electromotive force when the surface of this cell is exposed to light. The voltage generated can vary between 0.3 V and 0.7 V depending on the material used and its arrangement as well as the temperature and aging of the cell [3].

I.3.1. The different types of solar cells (photovoltaic cells):

There are four main types of cells:

a. Monocrystalline cells:

They have the best efficiency (from 12 to 18% or even up to 24% in the laboratory), however, they are too expensive due to their complex manufacturing process.

b. Polycrystalline cells:

They are easier to design and less expensive to manufacture. However, their efficiency is lower (from 11% to 15% or even up to 19.8% in the laboratory).

c. Amorphous cells:

They have a low efficiency (from 5% to 8% or even up to 13% in the laboratory), but require only very small thicknesses of silicon and are inexpensive. They are commonly used in small consumer products such as solar calculators or watches.

d. Perovskite solar cells:

They have higher energy conversion efficiency than traditional silicon-based cells in laboratory conditions, with values exceeding 25%. They are made from a class of materials with a specific crystal structure known as perovskite. These cells are relatively inexpensive to produce and offer great potential for future development due to their lightweight nature, flexibility, and ease of fabrication. However**,** Perovskite solar cells still face significant challenges, including poor environmental and thermal stability**,** potential toxicity due to the presence of lead**,** and limited long-term durability as their performance tends to degrade under real-world operating conditions**.** These issues currently hinder their widespread commercial adoption [4].

I.3.2. Efficiency:

Table (I-1) shows the efficiency of different types of photovoltaic cells [4].

Cell type	Efficiency	Lifetime	Characteristics
Mono-crystalline silicon	17-22%	20 to 30 Years	- Very good performance - High cost - Low efficiency under reduced illumination
Polycrystalline Silicon	16-18%	20 to 30 Years	- Performance/Price ratio - Low efficiency under reduced illumination.
Amorphous Silicon	6-11%	(+/- 10 Years)	- Operate with low illumination - Low manufacturing cost
Perovskite Silicon	20-25%	5 to 10 Years	- High efficiency - Low manufacturing cost - Poor stability and short lifespan - Sensitive to moisture and temperature

Table (I.1): Efficiency of different types of photovoltaic cells [4].

I.3.3. Electrical characteristics of a photovoltaic cell:

Figure (I.3) shows the equivalent diagram of a photovoltaic cell under illumination. It corresponds to a current generator I_{ph} mounted in parallel with a diode. Two parasitic resistances are introduced into this diagram.

These resistances have a certain influence on the characteristic I = f (V) of the cell [5]:

- **Series resistance (R_{ser}):** Represents the internal resistive losses within the solar cell. It primarily arises from the intrinsic resistance of the semiconductor material, the contact resistance at the interfaces between layers, and the sheet resistance of the metallic grid lines used for current collection.
- **Shunt resistance (R_{sh}):** Accounts for leakage currents that bypass the p–n junction, typically caused by manufacturing defects, impurities, or non-idealities in the cell structure. A high R_{sh} value is desirable, as it minimizes these leakage paths and improves cell efficiency.

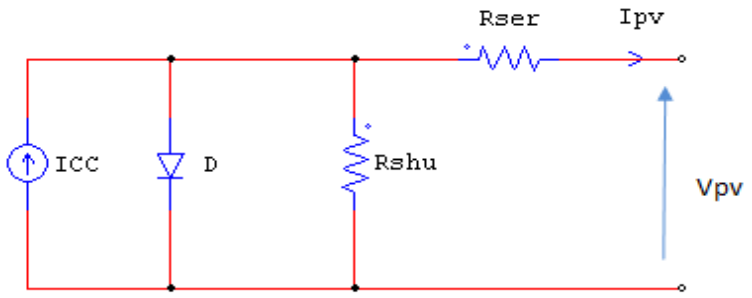


Figure (I.3): Equivalent electrical diagram of the photovoltaic cell [5].

The mathematical model for the current-voltage characteristic of a PV cell [5-7].

$$I_{pv} = I_{ph} - I_{sat}\left[\exp\frac{q\left(V_{pv}+(I_{pv}.R_{ser})\right)}{n.K.T} - 1\right] - \frac{\left(V_{pv}+(I_{pv}.R_{ser})\right)}{R_{shu}} \qquad (I.1)$$

- I_{sat} : Saturation current (A).
- K : Boltzmann's constant (1.3819×10^{-23} J/K).
- T : The effective cell temperature in Kelvin (K).
- q : The electron charge ($q=1.6\times10^{-19}$ C).
- n : Junction ideality factor ($1< n<3$).
- I_{pv} : The current supplied by the cell when operating as a generator.

- V_{pv} : The terminal voltage of the same cell.
- I_{ph} : Photocurrent of the cell, depending on illumination and temperature, or short-circuit current.
- R_{shu} : Shunt resistance characterizing junction leakage currents.
- R_{ser} : Series resistance representing the various contact and connection resistances.

I.3.4. Parameters of a photovoltaic cell:

These parameters can be determined from current-voltage curves or the characteristic equation, the most common are:

I.3.4.1. Short-circuit current (I_{sc}):

This is the current for which the voltage across the terminals of the cell or the PV generator [4] is zero. In the ideal case (R_{ser} zero and R_{shu} infinite), this current merges with the photo-current I_{ph}. In the opposite case, by canceling the voltage V in equation (I.2), we obtain:

$$I_{sc} = I_{ph} - I_{sat}\left[\exp\left(\frac{q\,(I_{sc}.R_{ser})}{n.K.T}\right) - 1\right] - \frac{(V_{pv} + (I_{sc}.R_{ser}))}{R_{shu}} \qquad (I.2)$$

For most cells (whose series resistance is low), the term can be neglected

$$I_{sat}\left[\exp\left(\frac{q\,(I_{sc}.R_{se})}{n.K.T}\right) - 1\right] \qquad (I.3)$$

The approximate expression for the short-circuit current is then:

$$I_{sc} = \frac{I_{ph}}{(1 + \frac{R_{ser}}{R_{shu}})} \qquad (I.4)$$

Quantitatively, it has the highest value of the current generated by the cell (practically $I_{sc} = I_{ph}$).

I.3.4.2. Open circuit voltage (V_{oc}):

This is the V_{co} voltage for which the current delivered by the photovoltaic generator is zero (this is the maximum voltage of a solar cell or a photovoltaic generator) [6].

$$0 = I_{ph} - I_{sat}\left[\exp\left(\frac{qV_{oc}}{nKT}\right) - 1\right] - \frac{V_{oc}}{R_{shu}} \quad (I.5)$$

I.3.4.3. Energy efficiency:

This is the ratio between the maximum electrical power supplied by the cell P_{max} (I_{opt}, V_{op}) and the incident solar power [8]. It is given by:

$$I_{sc} = \frac{P_{mpp}}{P_{inc}} \quad (I.4)$$

With P_{inc} is equal to the product of the illumination and the total surface area of the solar cells. This parameter reflects the quality of conversion of solar energy into electrical energy.

I.3.4.4. Fill factor:

The fill factor FF, also called curve factor, is the ratio between the maximum power supplied by the cell P_{max} (I_{opt}, V_{opt}) and the product of the short-circuit current I_{cc} by the open-circuit voltage V_{co} (i.e. the maximum power of an ideal cell). The form factor indicates the quality of the cell; the closer it is to unity, the more efficient the cell is. It is around 0.7 for efficient cells; and decreases with temperature. It reflects the influence of losses through the two parasitic resistances R_{ser} and R_{shu}. It is defined by [8]:

$$FF = \frac{P_{mpp}}{I_{sc}.V_{oc}} = \frac{I_{mpp}.V_{mpp}}{I_{sc}.V_{oc}} \quad (I.7)$$

I.3.4.5. The maximum power point P_{mpp}:

The maximum power point (MPP), denoted as P_{mpp}, is the operational point on the photovoltaic module's (I-V) curve where the product of current (I_{mpp}) and voltage (V_{mpp}) yields the highest possible power output. This point varies depending on irradiation, temperature, and the electrical characteristics of the cell. For effective operation, photovoltaic systems typically incorporate maximum power point tracking (MPPT) technologies to continually adjust operating conditions and maintain output at this optimal point [8].

$$P_{mpp} = I_{mpp}.V_{mpp} \quad (I.8)$$

I.4. Photovoltaic generator and its performance:

The photovoltaic generator is a set of equipment installed to exploit photovoltaic energy in order to satisfy the load needs. Depending on the desired power, the modules can be assembled into panels to constitute a "photovoltaic field". Connected to the receiver without any other element, the solar panel operates "as the sun does", that is to say that the electrical power supplied to the receiver is a function of the power of the sun [8].

I.4.1. Influence of the series association of PV cells:

When photovoltaic cells are connected in series, the total voltage increases proportionally to the number of cells while the current remains constant. The total open circuit voltage of the module is the sum of the voltages of individual cells. Series connection is advantageous when higher voltages are needed, but the overall performance can be significantly impacted by shading or failure of a single cell [8].

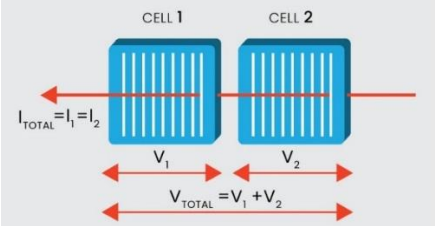


Figure (I.4): Mismatch for cells connected in series [8].

I.4.2. Influence of parallel association of PV cells:

When photovoltaic cells are connected in parallel, the total current output increases proportionally with the number of cells, while the voltage remains approximately equal to that of a single cell. Parallel configurations are used to increase the system current, providing more current at the same voltage, which is beneficial for systems requiring high current at lower voltage levels. However, differences in the characteristics of cells in parallel can lead to imbalanced currents [8].

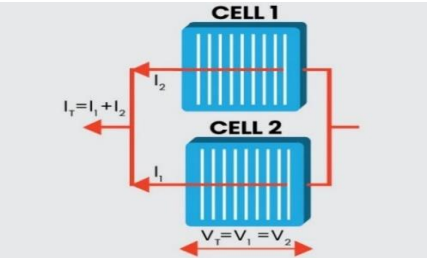


Figure (I.5): Mismatch for cells connected in parallel [8].

I.4.3. Influence of the mixed association (Series + Parallel) of PV cells:

A mixed association combines the benefits of both series and parallel connections. This configuration allows the system to achieve both higher voltage and higher current. The performance optimization must consider uniformity in cell characteristics, irradiation, and temperature to avoid significant mismatch losses [8].

For mixed configurations, the total voltage and current can be expressed as:

- **Series connection** increases voltage, so:

$$V_{total} = N_s . V_{cell} \quad (I.9)$$

- **Parallel connection** increases current, so:

$$I_{total} = N_p . I_{cell} \quad (I.10)$$

I.5. Photovoltaic panel:

A photovoltaic panel, or solar panel, is composed of multiple photovoltaic cells interconnected (in series and/or parallel) and encapsulated to withstand environmental conditions. Panels are equipped with protective layers such as tempered glass for physical protection and anti-reflective coatings to maximize energy capture. Each panel typically includes bypass diodes to mitigate shading effects and maintain performance [8].

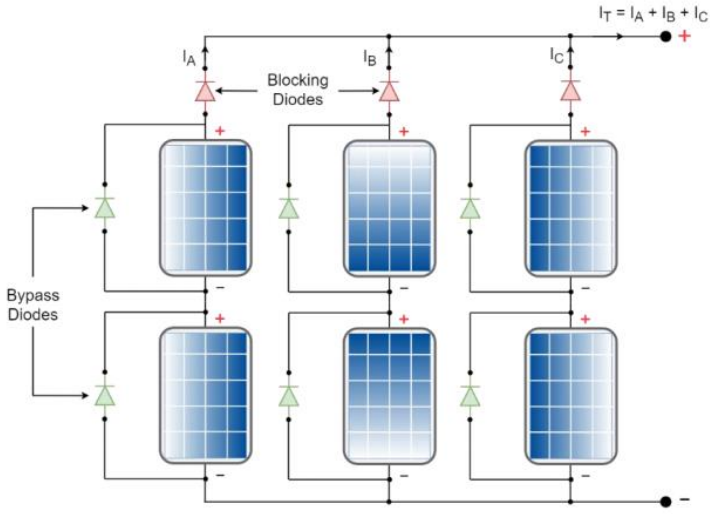


Figure (I.6): Modules protected by by-pass and blocking diodes [8]

The efficiency and performance of panels depend on [8]:

- Cell type (monocrystalline, polycrystalline, amorphous).
- Manufacturing quality and encapsulation methods.
- Environmental factors including dust, shading, temperature, and irradiation levels.

I.6 Photovoltaic (PV) System Simulation:

I.6.1 Current-Voltage Characteristic:

Figure (I.7) represents the $I = f(V)$ curve of a typical photovoltaic module under constant irradiation and temperature conditions.

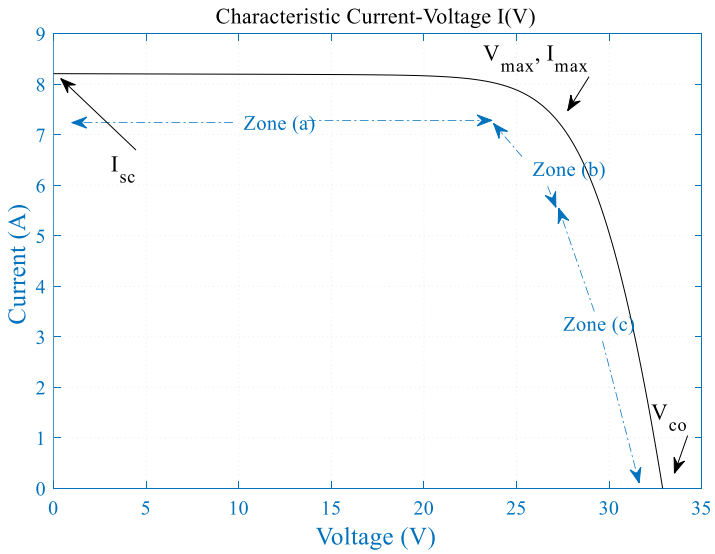


Figure (I.7): Characteristic I =f (V) of a photovoltaic module.

The characteristic is divided into three parts:

- Zone (a): where the current remains constant, the photovoltaic generator operates as a current generator.
- Zone (b): represents the preferred region for generator operation, where the optimum point (characterized by maximum power) can be determined.
- Zone (c): distinguished by a current variation corresponding to an almost constant voltage, in which case the generator can be likened to a voltage generator.

I.6.2 Power-voltage characteristic:

The power output (**P**) of a solar cell is determined by the product of the voltage (**V**) across the cell and the current (**I**) flowing through it, expressed by the equation: $P = V \times I$

By calculating the power for varying voltage values and plotting **P** against **V**, the power voltage (P–V) characteristic curve is obtained. This curve, commonly represented as $P = f(V)$ provides important insight into the operating performance of a photovoltaic cell, including the point at which maximum power is delivered known as the **Maximum Power Point (MPP).**

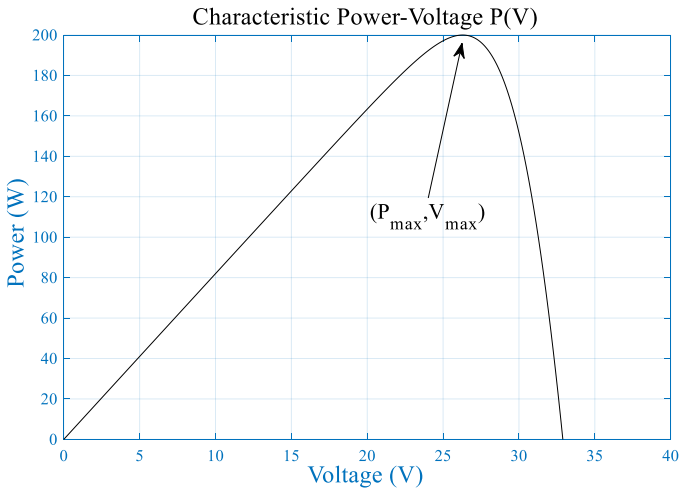


Figure (I-8): Power-Voltage Characteristic of PV module P=f (V)

I.6.3 Influence of illumination and temperature on the curves I=f (V) and P=f (V):

Figure (I.9) shows the influence of illumination on the characteristic I=f (V). At a constant temperature, we see that the current undergoes a significant variation, but on the other hand the voltage varies slightly. Because the short circuit current is a linear function of illumination while the open circuit voltage is a logarithmic function [4-6-8].

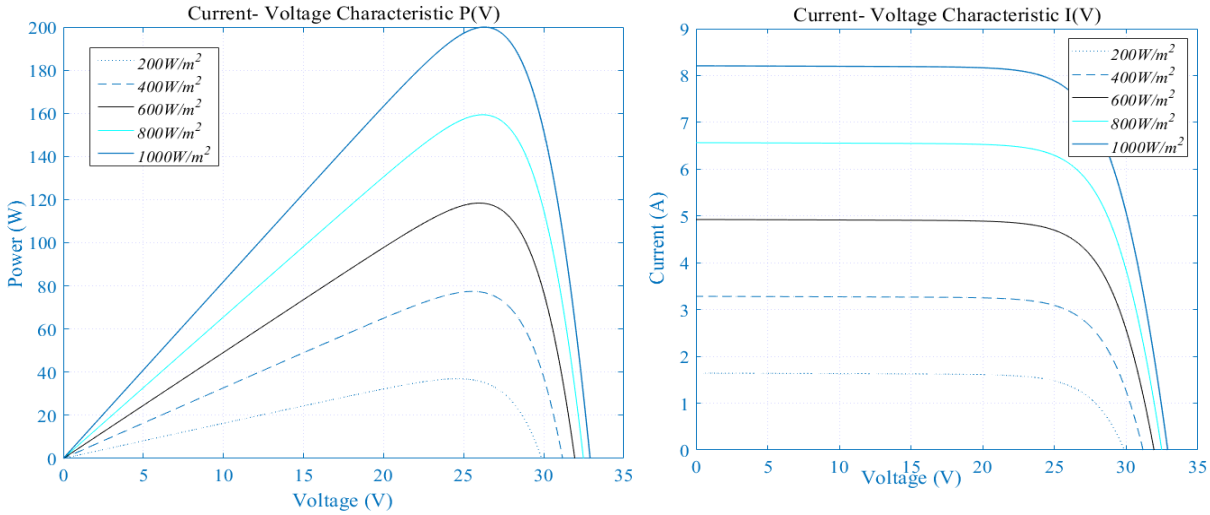


Figure (I.9): The influence of illumination on the characteristic I=f(V).

The same figure illustrates the variation of the power delivered by the generator as a function of the voltage for different illumination values, which allows us to deduce the influence of the illumination on the P (V) characteristic.

Figure (I.10) shows the influence of temperature on the I=f (V) characteristic. It is essential to understand the effect of changing the temperature of a solar cell on the I=f (V) characteristic. The current depends on the temperature since the current increases slightly as the temperature increases, but the temperature negatively affects the open circuit voltage. When the temperature increases the open circuit voltage decreases. Therefore, the maximum power of the generator undergoes a decrease.

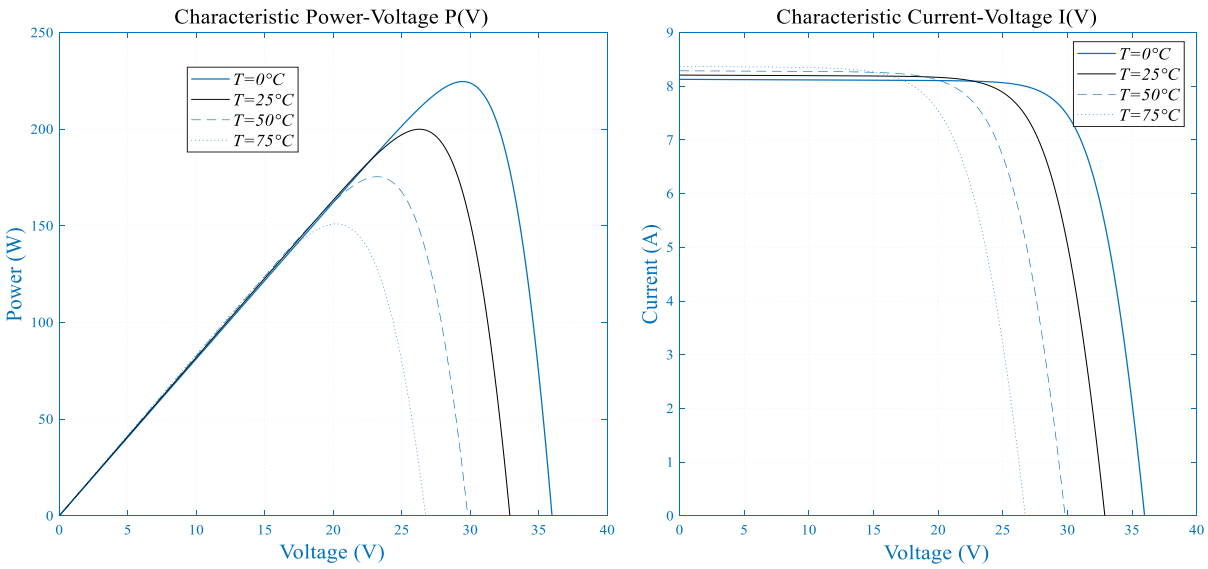


Figure (I.10): The influence of temperature on the characteristic I=f(V).

Figure (I.10) illustrates the variation in power output as a function of voltage for different temperatures, highlighting the impact of temperature on the P–V characteristic of the photovoltaic generator

I.6.4 Series-parallel association:

Connecting several cells in series forms a cell string, which increases the voltage for the same current while assembling several cell strings in parallel forms a module, which increases current and maintains voltage. An association of several modules in the same plane is called a panel, and the assembly of several panels in rows of series and parallel panels forms a photovoltaic field [9].

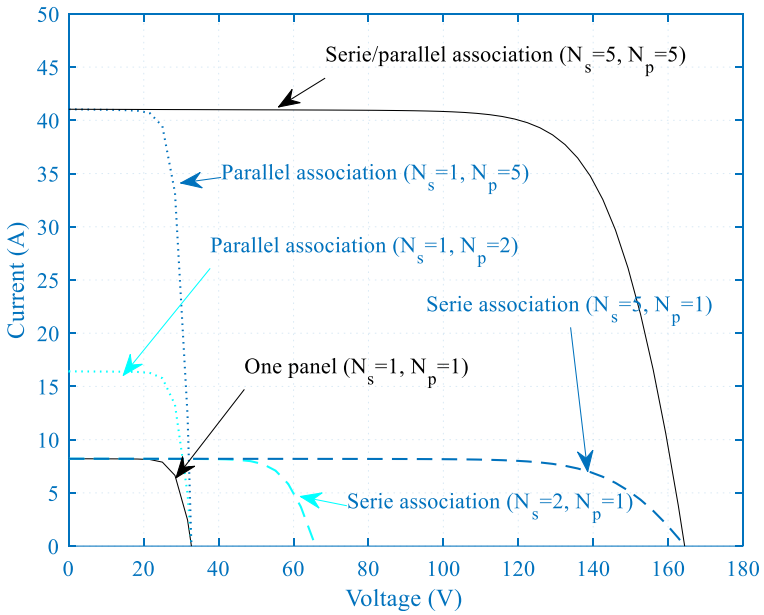


Figure I-11: Series-parallel association of PV cell.

I.7 Protection of photovoltaic system:

The standard outlines comprehensive requirements for the protection of photovoltaic (PV) systems, aiming to ensure safety, operational reliability, and adherence to established electrical installation codes. Key protection measures include:

I.7.1 Overcurrent Protection

PV circuits must be safeguarded against overcurrent's resulting from faults or abnormal operating conditions. Overcurrent protective devices (OCPDs), such as fuses or circuit breakers, should be installed to interrupt excessive currents and prevent damage to conductors and equipment. The sizing and placement of these devices must consider the maximum expected current and the characteristics of the PV modules and wiring.

I.7.2 Overvoltage Protection

Photovoltaic (PV) installations are vulnerable to overvoltages resulting from lightning strikes or switching operations. To safeguard the system against these transient events, surge protection devices (SPDs) should be implemented. The selection and coordination of SPDs must be appropriately matched to the system's voltage ratings and the specific conditions of the installation environment.

I.7.3 Ground Fault Protection

Ground faults, where current unintentionally flows to the ground, pose significant risks. PV systems must incorporate ground fault detection and interruption mechanisms to identify and isolate faults promptly, minimizing the risk of electric shock and fire.

I.7.4 Isolation and Switching

Proper isolation and switching devices are essential for maintenance and emergency situations. PV systems should include disconnecting means that allow for the safe isolation of circuits. These devices must be accessible and clearly marked to ensure safe operation and maintenance.

I.7.5 Protection against Electric Shock

To prevent electric shock hazards, PV installations must ensure adequate insulation, proper grounding, and the use of protective devices. The design should minimize the risk of direct or indirect contact with live parts, adhering to safety requirements for both normal operation and fault conditions.

I.7.6 Fire Protection

The risk of fire in PV systems can arise from faults such as short circuits or component failures. Protective measures include the use of fire-resistant materials, proper system design to prevent overheating, and the installation of devices that can detect and mitigate fault conditions promptly.

I.7.7 Environmental Protection

PV equipment must be protected against environmental factors like moisture, dust, and temperature extremes. Enclosures and components should have appropriate ingress protection (IP) ratings to withstand the specific environmental conditions of the installation site [10]

I.8 Shading:

Shading is one of the most critical factors that affect the performance and efficiency of photovoltaic (PV) systems. When part of a solar panel or array is shaded, even partially, it can significantly reduce the power output, sometimes disproportionately to the shaded area. This occurs because PV cells in a module are connected in series, and shading one cell can act like a bottleneck, limiting the current for the entire string.

I.8.1 Definition of Shading in PV Systems

Shading in photovoltaic (PV) systems refers to the partial or complete obstruction of sunlight on solar panels by external objects such as trees, buildings, dirt, or other panels. When sunlight is blocked from reaching the solar cells, the affected cells generate less or no electrical power, which reduces the overall output of the PV system [11].

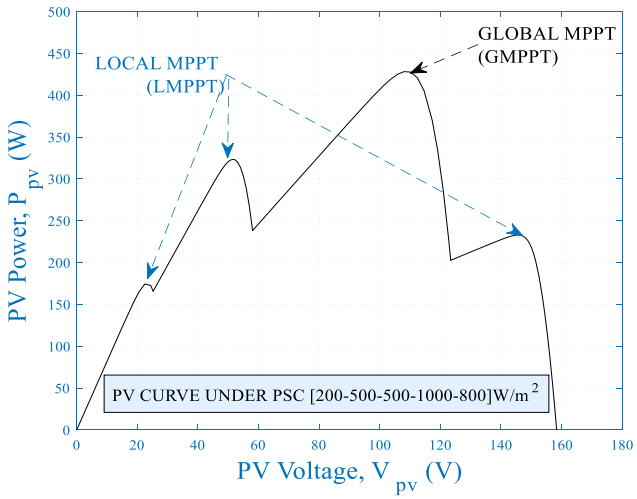


Figure I-12: Impact of partial shading on the P (V) characteristic.

I.8.2 Effects of Shading on PV Systems

- **Reduction in Power Output:** Even partial shading of a solar panel can cause a significant drop in the energy produced. This is because solar cells in a module are connected in series, and the current flow is limited by the cell receiving the least sunlight.
- **Mismatch Losses:** When shaded cells produce less current than unshaded ones, it creates electrical mismatches in the circuit, leading to inefficient operation and decreased system performance.
- **Hot Spots:** Shaded cells can become reverse-biased and dissipate power as heat, creating "hot spots" that may damage the solar panel over time.
- **Decreased System Reliability:** Continuous shading can cause premature degradation of modules, reducing their lifespan and increasing maintenance costs.
- **Economic Impact:** Reduced energy production due to shading translates to lower returns on investment and higher levelized cost of energy (LCOE) [12].

I.9 Advantages and Drawbacks of Photovoltaic Energy:

I.9.1 Advantages:

- **Renewable and Sustainable:** PV energy is derived from sunlight, a limitless and renewable resource, making it a sustainable energy option.
- **Environmentally Friendly:** It produces no direct greenhouse gas emissions or air pollutants during operation, reducing carbon footprint.
- **Low Operating Costs:** After installation, PV systems have minimal operating and maintenance costs.
- **Scalability and Flexibility:** PV systems can be deployed at various scales, from small residential rooftops to large utility-scale solar farms.
- **Energy Independence:** Utilizing PV energy reduces dependence on fossil fuels and enhances energy security.
- **Job Creation:** The solar industry creates employment opportunities in manufacturing, installation, and maintenance.

I.9.2 Drawbacks:

- **Intermittency:** PV power generation depends on sunlight availability, causing fluctuations due to weather and day-night cycles.
- **High Initial Cost:** The upfront cost of PV panels and installation remains relatively high despite decreasing prices.
- **Land and Space Requirements:** Large-scale PV farms require significant land area, which can impact land use and ecosystems.
- **Energy Storage Needs:** To provide reliable power, especially when sunlight is not available, costly storage solutions like batteries are often required.
- **Material and Resource Constraints:** Manufacturing PV panel involves the use of rare or hazardous materials that need careful handling and recycling [13].

I.10 Conclusion:

This chapter introduced the basics of photovoltaic (PV) systems, including their structure, types of solar cells, and key operating principles. We examined electrical characteristics like current-voltage behavior, efficiency, and the impact of environmental factors such as irradiation and temperature. Different connection methods and protection mechanisms were also discussed, along with the effects of shading. While PV systems offer many benefits like sustainability and low emissions, they also face challenges such as intermittency and high initial costs. This overview provides a solid foundation for understanding and improving PV system performance.

Chapter II:

DC-DC Converters

II.1.Introduction:

In this chapter, we introduce the fundamental principles of switching power conversion and examine various types of DC-DC converter circuits. We focus on the buck, boost, and buck-boost converters, deriving mathematical models that describe both their steady-state and dynamic behavior. A typical converter switching stage includes capacitors, inductors, and semiconductor switches. These components ideally do not consume energy, which contributes to the high efficiency of switching converters. The switch is usually implemented using a semiconductor device operating in switched mode, most commonly a MOSFET (metal-oxide-semiconductor field-effect transistor).

This chapter provides a comprehensive overview of DC-DC converter topologies along with their mathematical modeling, offering insights into both circuit-level performance and dynamic response.

II.2. DC-DC Converters (Choppers):

Solar energy is an intermittent energy source, with availability fluctuating significantly throughout the day. To utilize it efficiently, the nature of the connected loads, such as batteries, lighting systems, and other devices must be taken into account. In this context, several researchers have employed boost converters to enhance energy harvesting and optimize system performance. This work aims to present an improved boost converter design capable of continuously tracking and extracting maximum power, regardless of variations in solar irradiance [23-24].

II.2.1. Modeling of the Boost Converter:

The boost converter or parallel chopper known as the step-up voltage converter, is shown in Figure (II.1). It is generally used in converting a low input voltage into a higher output voltage. It consists of a continuous input voltage source , an inductor L, a switch S, a diode, and two capacitors C_{in} and C_{out}. Initially, in the interval $[0, \alpha T]$,the transistor is closed, the current in the inductor increases gradually, and it stores energy. At the end of the first period, the transistor opens and the inductor resists the decrease in current I; thus, it generates a voltage that adds to the source voltage and is applied to the load through the diode [13].

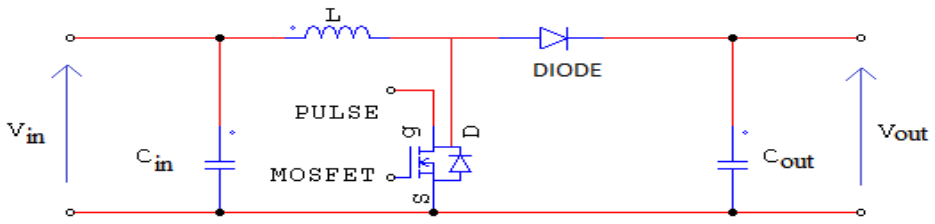


Figure (II.1): Electrical schematic of the boost converter [13].

Applying Kirchhoff's laws to the two equivalent circuits of the boost converter shown in Figure (II.2) for both operating phases gives [13]:

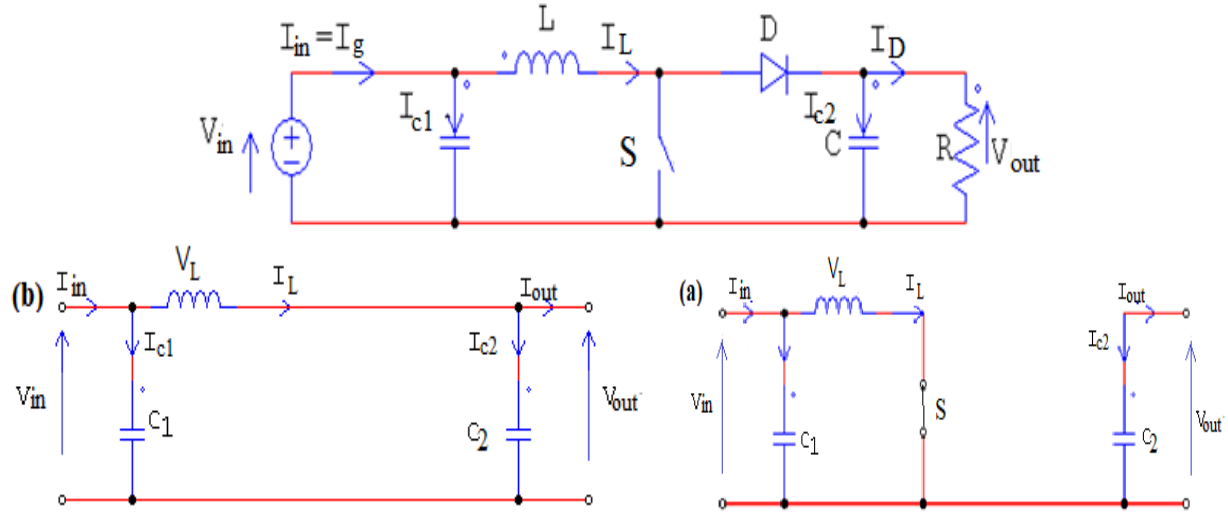


Figure (II.2): Equivalent schematics of the boost chopper [13].

For the first period αT_s :

$$\begin{cases} I_{c1} = C_1 \dfrac{dV_{in}}{dt} = I_{in} - I_L \\ I_{c2} = C_2 \dfrac{dV_{out}}{dt} = -I_{out} \\ V_L = L \dfrac{dI_L}{dt} = V_{in} \end{cases} \quad \text{(II.1)}$$

For the second period (1-α) T_s :

$$\begin{cases} I_{c1} = C_1 \dfrac{dV_{in}}{dt} = I_{in} - I_L \\ I_{c2} = C_2 \dfrac{dV_{out}}{dt} = I_L - I_{out} \\ V_L = L \dfrac{dI_L}{dt} = V_{in} - V_{out} \end{cases} \quad \text{(II.2)}$$

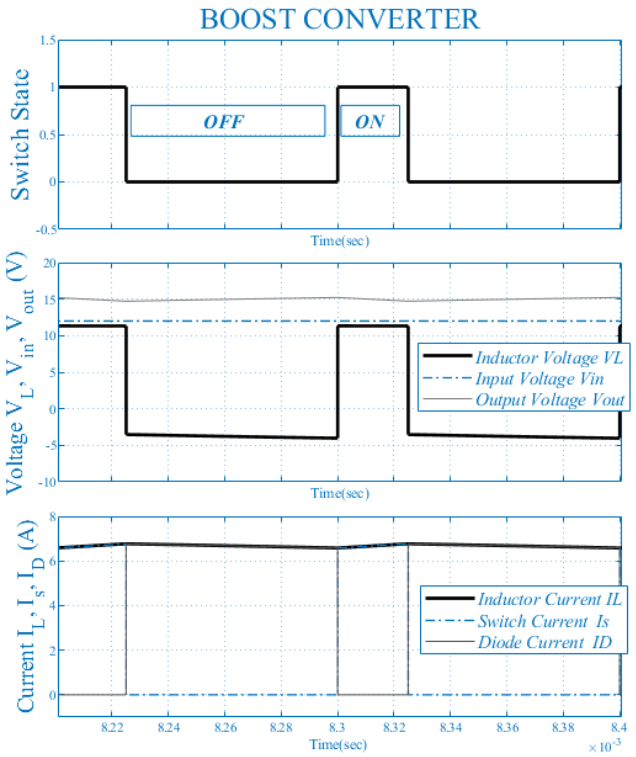


Figure (II.3): Voltage and current characteristics of the boost converter.

II.2.2. Modeling of the Buck Converter (Step-Down):

Figure (II.5) shows the buck converter or step-down converter (voltage reducer) or series chopper. Its main role is to convert its input voltage into a lower output voltage [14].

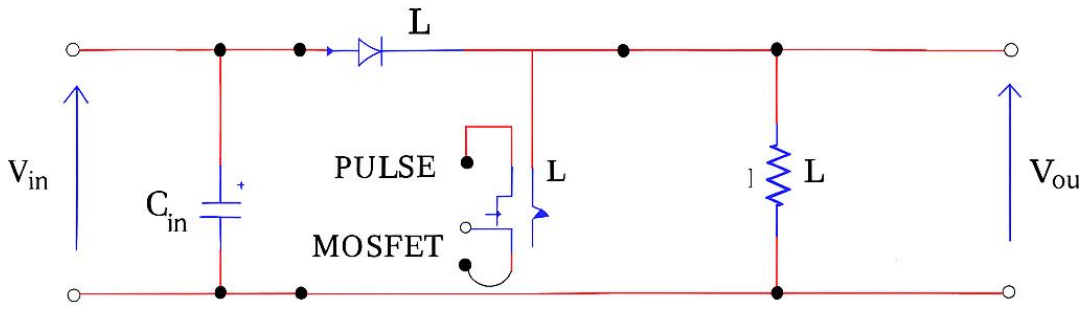


Figure (II.4): Electrical schematic of the Buck converter [14].

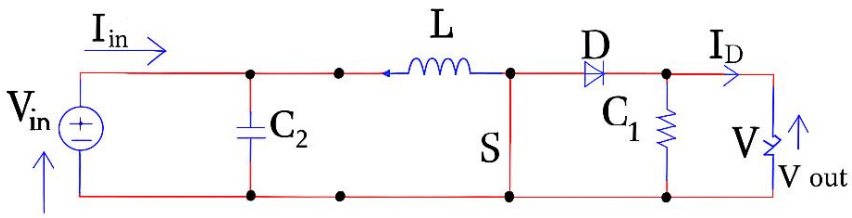


Figure (II.5): Equivalent schematics of the Buck chopper.

The key components are the inductor L, the transistor switch S, the diode D, and the capacitorC. The capacitor charges through the switch S and maintains the voltage across its terminals until S opens, at which point it discharges its energy through the diode to the load during one switching cycle. The switch can be a MOSFET transistor or an IGBT, which can switch rapidly between two states: ON or OFF. The source voltage must be greater than the voltage across the load [15].

The mathematical equation characterizing the current in the inductor is given by the following equation:

$$\frac{\delta I}{\delta t} = \frac{V_{in} - V_{out}}{L} \qquad \text{(II.22)}$$

I_L : The current in the inductor. The switching process is described by the position of the switch S . During the first interval αT , the transistor is in saturation state, so the inductor L stores energy with increasing current [15]. During the second interval $(1-\alpha)T$, the inductor L releases this energy to the load with decreasing current. Neglecting the voltage drop across the diode, the rate of change of the current is given by:

$$\frac{\delta I}{\delta t} = \frac{V_{in}}{L} \qquad \text{(II.23)}$$

When the inductor current does not decrease to zero before the transistor switches again, the converter operates in continuous conduction mode, as illustrated in Figure (II.5). In this case, if the load voltage depends only on the source voltage and the duty cycle $\alpha = \frac{T_{on}}{T}$ then the voltage across the load is ($V_{out} = \alpha V_{in}$). In discontinuous conduction mode, the current through the inductor falls to zero during a switching cycle between the transistor S and the diode. In this case, the load voltage depends in a more complex manner on the duty cycle and the load current. Figure (II.7) shows how the load voltage varies with the load current [15]. The current and voltage characteristics representing the operation of the buck converter are given in Figure (II.6):

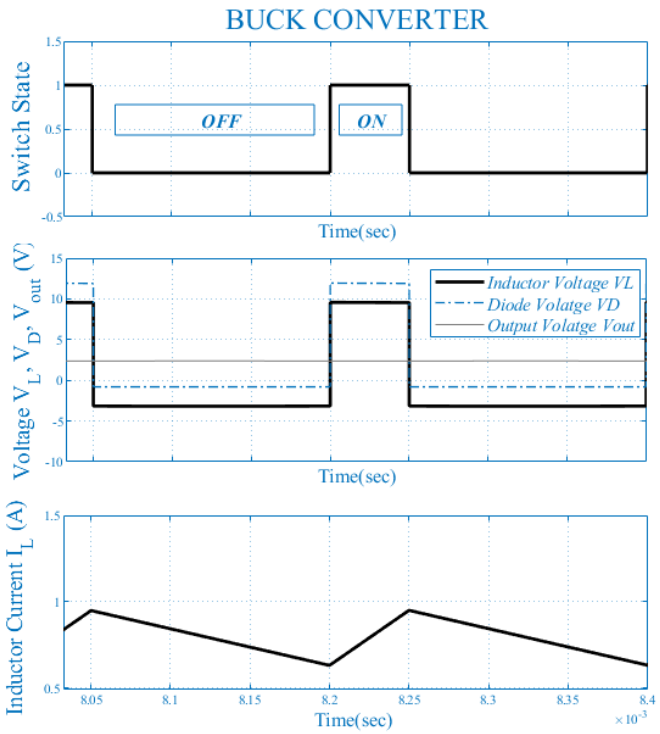


Figure (II.6): Voltage and current characteristics of the buck converter.

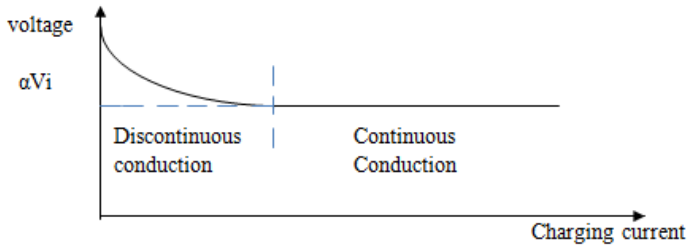


Figure (II.7): Variation of the load voltage with the load current for a Buck Converter [15].

II.2.3. Modeling of the Buck-Boost Converter

The buck-boost converter combines the properties of buck and boost configurations. It can ideally be used to convert any DC input voltage into any desired DC output voltage [15].

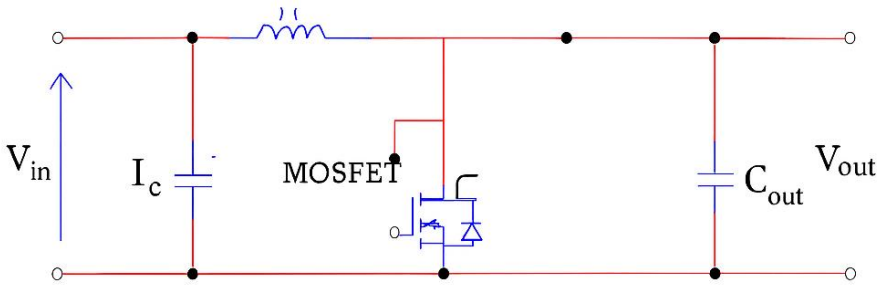


Figure (II.8): Electrical diagram of a buck-boost converter [15].

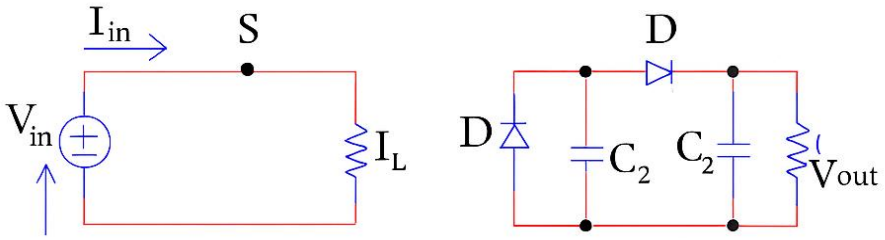


Figure (II.9): Equivalent schematics of the Buck-boost chopper.

Figure (II.8) shows the schematic of the basic electrical circuit of the buck-boost converter, along with the characteristics of the current and the load voltage in this device. The voltage can be increased or decreased depending on the switching mode. However, the output voltage has the opposite sign of the input voltage [16]. When the transistor is in the ON position, the current through the inductor increases and energy is stored; and when the switch turns to the OFF position, the voltage across the inductor is reversed, and the stored energy is transferred to the load via the diode. In this case, the equation for the voltage across the load, describing operation in continuous conduction mode, is given as follows:

$$V_{out} = \frac{\alpha}{1-\alpha} . V_{in} \qquad \text{(II.24)}$$

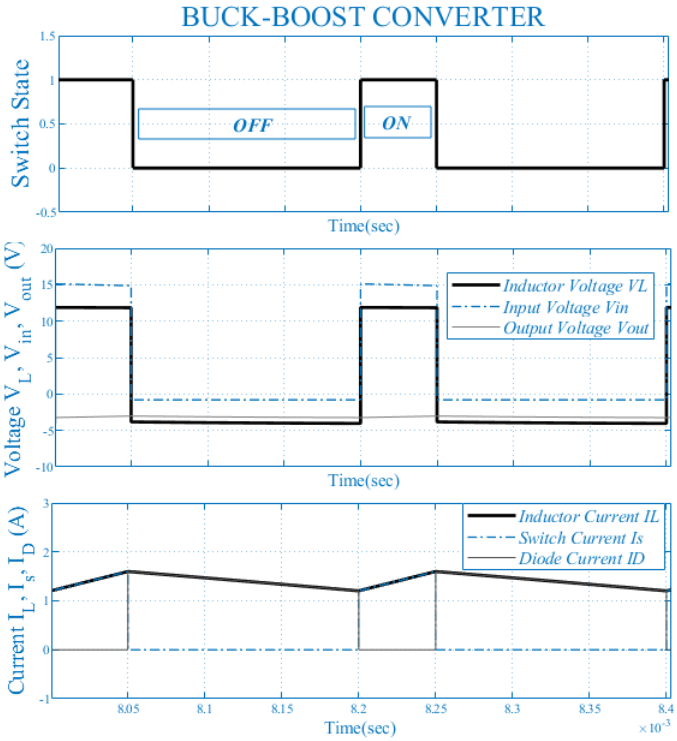


Figure (II.10): Voltage and current characteristics of the buck-boost converter.

II.3 MPPT-Control

MPPT control maximizes the energy extraction from solar panels, improving the overall efficiency and performance of the PV system. It adapts to changing environmental conditions, ensuring optimal power output throughout the day and across different seasons. This control system is used in DC-DC converters that automatically adjust the duty cycle α to the optimum value, there by maximizing the power output of the PV panel. The MPPT algorithm can be simple or complex depending on the method used to find the MPP (Maximum Power Point). For this reason, the most popular control algorithms are presented and discussed below. [26]

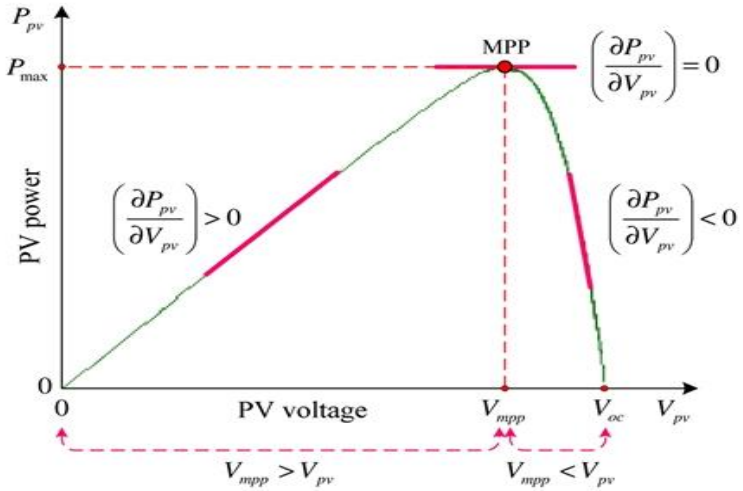


Figure (II.11): Principle of MPPT control

II.3.1 MPPT Control Classification

MPPT (Maximum Power Point Tracking) methods are categorized into **indirect** and **direct** approaches, depending on how they determine the maximum power point (MPP) of a photovoltaic (PV) system.

II.3.2 Indirect MPPT Methods

Indirect methods estimate the MPP using known relationships between PV parameters, such as:

- **Open-Circuit Voltage (OCV)**: $Vmpp = K * Voc$
- **Short-Circuit Current (SCC)**: $Impp = K * Isc$
- **Look-Up Tables**: Use pre-stored data based on environmental conditions

These methods are simple and low-cost but less accurate and panel-dependent [17]

II.3.3 Direct MPPT Methods

Direct methods measure PV voltage and current in real time to locate the MPP:

- **Perturb and Observe (P&O)**: Adjusts the operating point and observes power changes
- **Incremental Conductance (IncCond)**: Compares $\frac{\Delta I}{\Delta v}$ with $\frac{-I}{v}$
- **Fuzzy Logic**: Uses adaptive rules based on system behavior [28].

II.4 Conclusion:

This chapter presented the main types of DC-DC converters buck, boost, and buck-boost explaining their operation, modeling, and relevance in renewable energy systems, particularly solar power. Each converter's behavior in different conduction modes was analyzed, highlighting how they regulate voltage using switching components. The chapter also discussed MPPT techniques, both direct and indirect, which are essential for optimizing energy extraction from PV panels.

Chapter III:

Modeling of Induction Machine

III.1 Introduction:

The asynchronous machine is highly valued in industrial environments for its robustness, high specific torque, and low production cost. It now appears to be the basic element of high-performance electric actuators [18]. The representation of the mathematical model in dynamic form of the asynchronous machine allows the observation and analysis of the various evolutions of its electromechanical quantities on the one hand and the development of control laws on the other hand, and to predict the necessary control [19].

The main goal of this chapter is to model an asynchronous machine powered by a three-phase voltage inverter. First, we present the basic models used for a voltage-supplied machine, followed by simulation of the behavior of the induction motor supplied by two levels inverter.

III.2 Overview of the Asynchronous Machine:

III.2.1 Definition:

The asynchronous machine is an alternating current machine, the rotor speed and the speed of the rotating magnetic field are not equal because of the slip. The rotor is always behind the stator field, the asynchronous machine is called (induction machine) because the energy is transferred from the stator to the rotor or vice versa by electromagnetic induction [20].

III.2.2 Composition of the asynchronous machine:

The asynchronous machine consists of the following main elements (See Figure (III.1)):

- The stator (fixed part) consisting of magnetic lamination discs carrying the windings responsible for magnetizing the air gap;
- The rotor (rotating part) consisting of magnetic lamination discs stacked on the machine shaft carrying an injected winding;
- The mechanical components allowing the rotor to rotate and maintaining the various sub-assemblies [21-22].

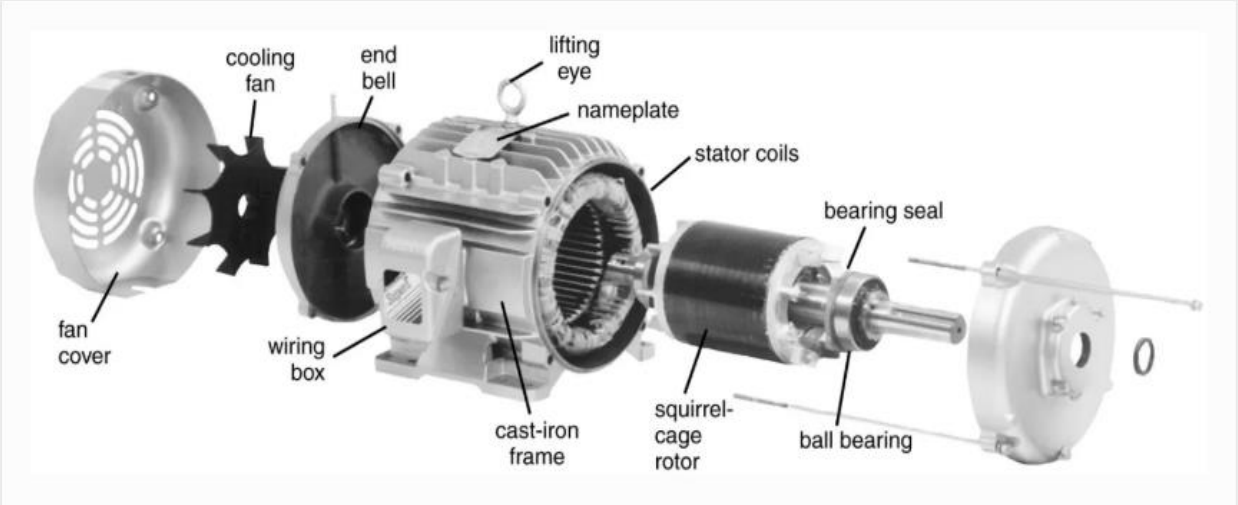


Figure (III.1): Asynchronous (induction) motor.

III.2.2.1 Stator:

The stator is the fixed part of the machine; it consists of wound coils distributed in the slots of the magnetic circuit. This magnetic circuit consists of a stack of metal sheets in which slots parallel to the machine axis are cut (see Figure (III.2)).

The stator winding can be divided into two parts: the slot conductors and the coil heads. The slot conductors create the magnetic field in the air gap that causes the electromagnetic conversion. The coil heads, for their part, allow the currents to close by organizing the judicious flow of currents from one slot conductor to the other [21-22].

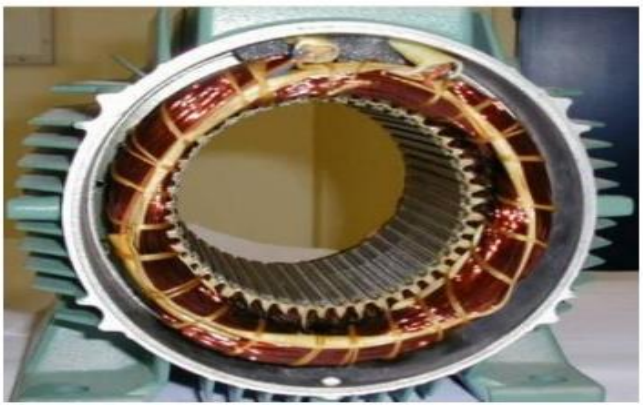


Figure (III.2): Stator of the asynchronous machine.

This stator powered by three-phase currents creates a magnetic field rotating at synchronous speed [21]:

$$N_s = \frac{f}{p} \quad \text{(III.1)}$$

Where:

- N_s : Synchronous rotational speed of the rotating field.
- f : Frequency (Hz).
- p : Number of pole pairs.

III.2.2.2 Rotor:

The rotor is not connected to any power supply. It rotates at the rotational speed (n). This winding is also called the "armature." [22]. It comes in two forms:

- Squirrel-cage rotor (see Figure (III.3)).
- Wound rotor (see Figure (III.5)).



Figure (III.3): Squirrel-cage rotor.

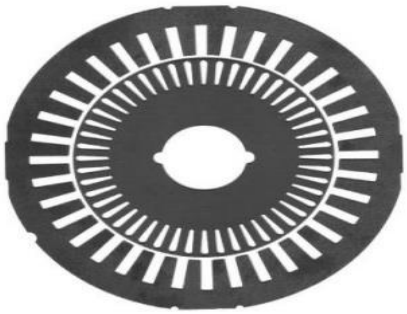


Figure (III.4): Magnetic circuit.

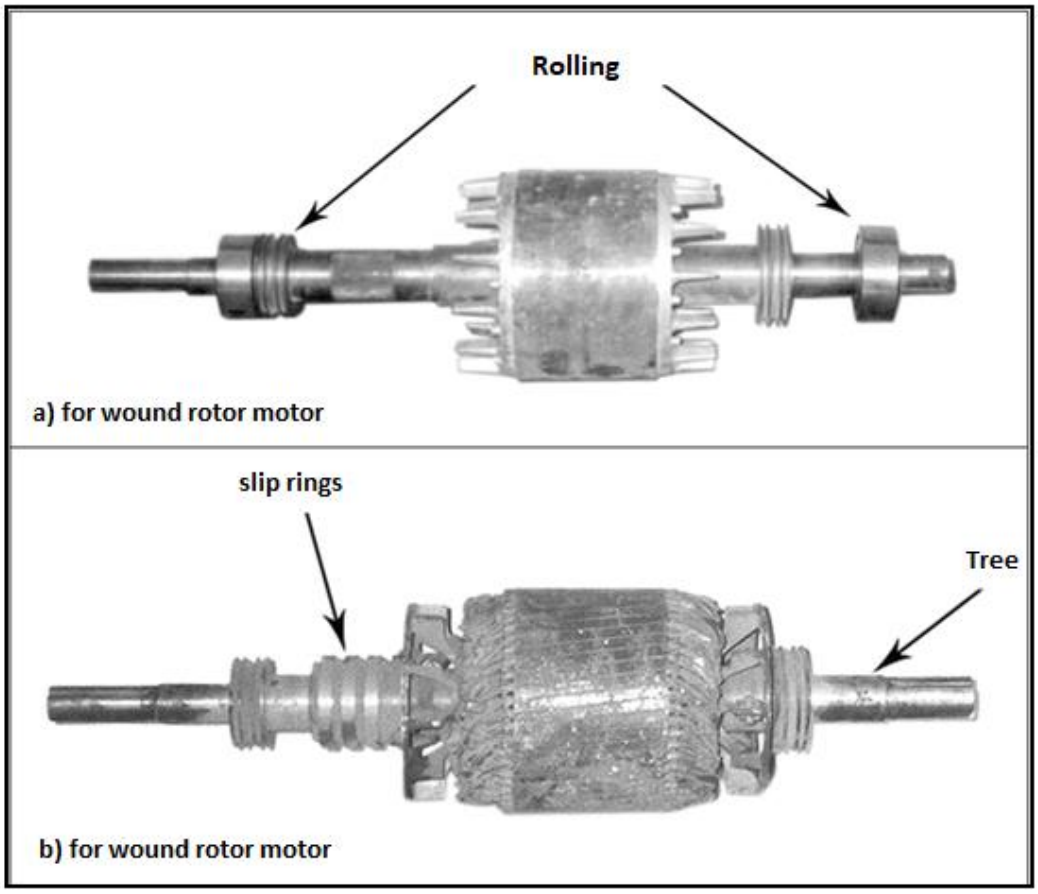


Figure (III.5): Wound rotor.

III.3 Representation of the three-phase asynchronous machine in electrical space:

The asynchronous machine has six windings, three in the stator supplied by a three-phase current and three in the short-circuited rotor. The stator windings are phase-shifted by an electrical angle of $\frac{2\pi}{3}$ relative to each other in space (Figure III.6) [22].

Where:

θ_r : Is the electrical mechanical angle between the axis of the stator phase and the rotor phase:

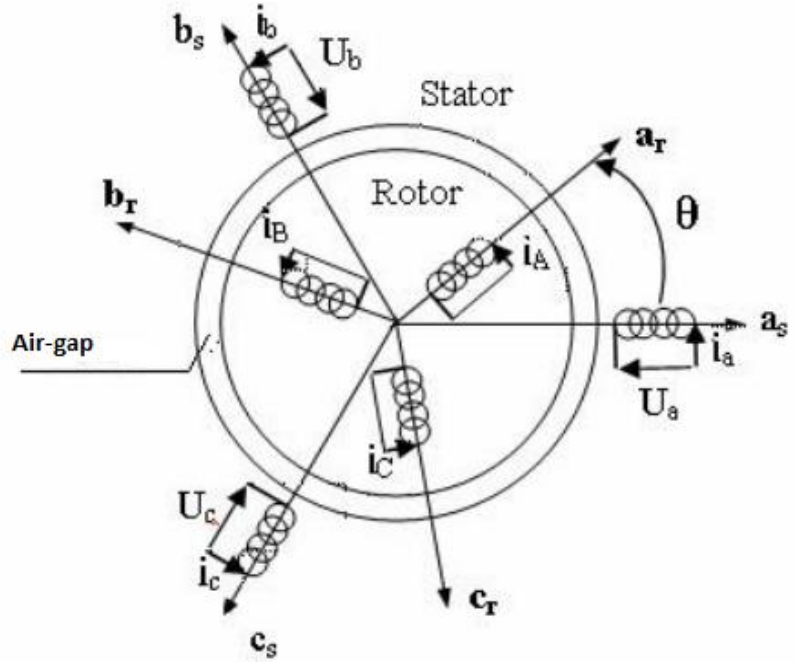


Figure (III.6): Representation of the three-phase asynchronous machine in electrical space.

The operating principle is based entirely on the laws of induction:

- The asynchronous machine behaves like a transformer who's secondary (rotor) is short-circuited.
- The synchronous speed N_s of the rotating field generated by the stator is directly proportional to the frequency f of the three-phase supply voltage [23].

$$Ns = 120.\frac{f}{p} \qquad \text{(III.2)}$$

When the rotor rotates at a speed Ω_r different from Ω_s (asynchronous), applying FARADAY's law [23] to the rotor windings reveals that they become the site of a system of three-phase electromotive forces, which in turn generate three rotor currents. According to LENZ's law, these currents oppose the cause that produced them, namely, the relative motion between the rotating stator magnetic field and the rotor [24]. As results, the rotor is driven in the direction of the rotating field, attempting to reach the synchronous speed Ω_s, such that:

$$\Omega_s = \frac{\omega_s}{p} \qquad \text{(III.3)}$$

And the rotor rotates at a speed Ω_r, with:

$$\Omega_r = \frac{\omega_r}{p} \tag{III.4}$$

Since this speed is lower than Ω_s, the rotor is not in synchronism with the rotating magnetic field; hence, the machine is referred to as asynchronous.

Therefore, depending on whether Ω_r is lower (hypo synchronous) or higher (hyper synchronous) than Ω_s, the machine develops respectively a motor torque tending to increase Ω_r, or a resistive torque tending to reduce Ω_r, obviously the electromagnetic torque is cancelled at equal speed. The energy exchange with the network gives the sign of the difference (Ω_s -Ω_r). Asynchronous operation is thus characterized by the slip "g" defined by [25]:

$$g = \frac{\Omega s - \Omega r}{\Omega s} \tag{III.5}$$

III.4 Modeling the asynchronous machine:

III.4.1 Simplifying assumptions:

The study of the asynchronous machine translates the laws of electromagnetism into the usual context of simplifying assumptions: [25]

- Constant air gap,
- Neglected cogging effect,
- Sinusoidal spatial distribution of magneto-motive forces in the air gap,
- Unsaturated magnetic circuit with constant permeability,
- Negligible ferromagnetic losses,
- Winding resistances do not vary with operating temperature, and the skin effect is also neglected.

Important consequences of these assumptions include [26]:

- Constant self-inductances,
- Magnetic flux is a linear function of current,
- Invariance of stator and rotor resistances,
- Mutual inductances between stator and rotor windings as a function of the electrical angle of their magnetic axes.

III.4.2 Equations of the Generalized Asynchronous Machine:

The behavior of the IM is defined by three types of equations

a) Electrical equations.
b) Magnetic equations.
c) Mechanical equations.

III.4.3. Electrical Equations:

By applying Ohm's law, the voltage equations of the three stator and rotor phases are given respectively by:

$$V_{as} = R_s i_{as} + \frac{d}{dt}\varphi_{as} \quad \text{(III.6)}$$

$$V_{bs} = R_s i_{bs} + \frac{d}{dt}\varphi_{bs} \quad \text{(III.7)}$$

$$V_{cs} = R_s i_{cs} + \frac{d}{dt}\varphi_{cs} \quad \text{(III.8)}$$

$$V_{ar} = R_r i_{ar} + \frac{d}{dt}\varphi_{ar} \quad \text{(III.9)}$$

$$V_{br} = R_r i_{br} + \frac{d}{dt}\varphi_{br} \quad \text{(III.10)}$$

$$V_{cr} = R_r i_{cr} + \frac{d}{dt}\varphi_{cr} \quad \text{(III.11)}$$

In matrix form, equations (III.6-III.11) can be written:

$$[V_{abcs}] = [R_s][i_{abcs}] + \frac{d}{dt}[\varphi_{abcs}] \quad \text{(III.12)}$$

$$[V_{abcr}] = [R_r][i_{abcr}] + \frac{d}{dt}[\varphi_{abcr}] \quad \text{(III.13)}$$

With:

$$[R_s] = \begin{bmatrix} R_s & 0 & 0 \\ 0 & R_s & 0 \\ 0 & 0 & R_s \end{bmatrix}, [R_r] = \begin{bmatrix} R_r & 0 & 0 \\ 0 & R_r & 0 \\ 0 & 0 & R_r \end{bmatrix} \quad \text{(III.14)}$$

And:

$$[V_{abcs}] = [V_{as} V_{bs} V_{cs}]^T \quad , \quad [V_{abcr}] = [V_{ar} V_{br} V_{cr}]^T \tag{III.15}$$

$$[i_{abcs}] = [i_{as} i_{bs} i_{cs}]^T \quad , \quad [i_{abcr}] = [i_{ar} i_{br} i_{cr}]^T \tag{III.16}$$

III.4.4 Magnetic equation:

The magnetic equations between fluxes and currents are [27]:

$$[\phi_{abcs}] = [L_{ss}][i_{abcs}] + [L_m][i_{abcr}] \tag{III.17}$$

$$[\phi_{abcr}] = [L_{rr}][i_{abcr}] + [L_m][i_{abcs}] \tag{III.18}$$

With:

$$[\phi_{abcs}] = \begin{bmatrix} \phi_{as} \\ \phi_{bs} \\ \phi_{cs} \end{bmatrix} \tag{III.19}$$

$$[\phi_{abcr}] = \begin{bmatrix} \phi_{ar} \\ \phi_{br} \\ \phi_{cr} \end{bmatrix} \tag{III.20}$$

Or:

$[\phi_{abcs}]$: Stator flux matrix,

$[\phi_{abcr}]$: Rotor flux matrix.

The stator and rotor inductance matrices are given by:

$$[L_{ss}] = \begin{bmatrix} l_s & L_s & L_s \\ L_s & l_s & L_s \\ L_s & L_s & l_s \end{bmatrix} \tag{III.21}$$

$$[L_{rr}] = \begin{bmatrix} l_r & L_r & L_r \\ L_r & l_r & L_r \\ L_r & L_r & l_r \end{bmatrix} \tag{III.22}$$

$$[L_m] = L_m \begin{bmatrix} \cos\theta & \cos(\theta + \frac{2\pi}{3}) & \cos\left(\theta - \frac{2\pi}{3}\right) \\ \cos(\theta - \frac{2\pi}{3}) & \cos\theta & \cos(\theta + \frac{2\pi}{3}) \\ \cos(\theta + \frac{2\pi}{3}) & \cos(\theta - \frac{2\pi}{3}) & \cos\theta \end{bmatrix} \quad \textbf{(III.23)}$$

Or:

$[L_m]$: Represents the matrix of mutual inductances between stator and rotor. The inductance between the rotor and stator is considered identical:

$$[L_m] = [L_m]^T \quad \text{(III.24)}$$

III.4.5 Mechanical equation:

The mechanical equation of the machine is given by:

$$J \frac{d\Omega}{dt} = T_{em} - T_r - f_c.\Omega \quad \text{(III.25)}$$

With:

- T_{em} : Electromagnetic torque.
- T_r : Resistive torque.
- f_c : Friction coefficient.
- J : Rotor moment of inertia.

The equations of the asynchronous machine are given as follows:

$$[V_{sabc}] = [R_s][i_{sabc}] + \frac{d}{dt}([L_{ss}][i_{sabc}] + [L_m].[i_{rabc}]) \quad \text{(III.26)}$$

$$[V_{rabc}] = [R_r][i_{rabc}] + \frac{d}{dt}([L_{rr}][i_{rabc}] + [L_m].[i_{sabc}]) \quad \text{(III.27)}$$

This presentation of three-phase modelling has one major drawback for our application: the matrices [Lm] depend on the mechanical rotation angle θ and must therefore be recalculated at each sampling step, to remedy this problem, we carry out transformations [27].

III.5 Three-phase/diphase transformations:

The purpose of using this transformation is to simplify the study of IM. Indeed, we go from a three-phase abc system to a two-phase α,β, or $d-q$ system. There are mainly three transformations:

- The Clark transformation.
- The Concordia transformation.
- The Park transformation.

III.5.1 Clark transformation :

The Clark transformation is a mathematical tool used in electrical engineering, and in particular for vector control, to model a three-phase system using a base traditionally named αβ [26-27]. Transformed values are generally currents, voltages or fluxes such as:

$$\begin{bmatrix} X_\alpha \\ X_\beta \\ X_0 \end{bmatrix} = \frac{2}{3}\begin{bmatrix} 1 & \cos\left(\frac{2\pi}{3}\right) & \cos\left(\frac{2\pi}{3}\right) \\ 0 & \sin\left(\frac{2\pi}{3}\right) & \sin\left(\frac{2\pi}{3}\right) \\ \frac{1}{2} & \frac{1}{2} & \frac{1}{2} \end{bmatrix}\begin{bmatrix} X_a \\ X_b \\ X_c \end{bmatrix} \qquad \text{(III.28)}$$

III.5.2 Concordia transformation:

The Concordia transform [26-27] is very similar to the Clark transform, except that it is unitary. The powers after transformation are therefore the same as in the initial system, which is not the case for the Clark transform.

$$\begin{bmatrix} X_\alpha \\ X_\beta \\ X_0 \end{bmatrix} = \sqrt{\frac{2}{3}}\begin{bmatrix} 1 & \cos\left(\frac{2\pi}{3}\right) & \cos\left(\frac{2\pi}{3}\right) \\ 0 & \sin\left(\frac{2\pi}{3}\right) & \sin\left(\frac{2\pi}{3}\right) \\ \frac{1}{\sqrt{2}} & \frac{1}{\sqrt{2}} & \frac{1}{\sqrt{2}} \end{bmatrix}\begin{bmatrix} X_a \\ X_b \\ X_c \end{bmatrix} \qquad \text{(III.29)}$$

The (α) axis is coincident with the (a) axis.

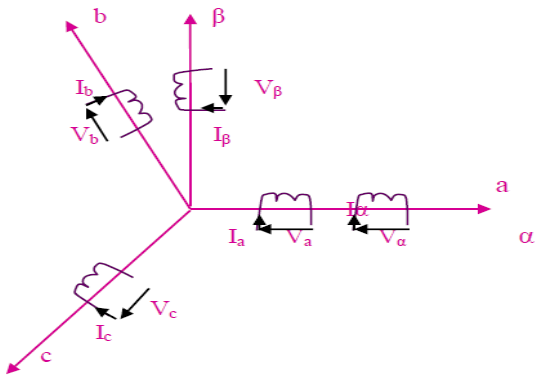


Figure (III.7): Transformation from Three-Phase (abc) to Concordia ($\alpha\beta$) Frame**.**

III.5.3 Park transformation:

The Park transformation is is commonly known as a two-axis transformation. Physically, the application of this transformation to the IM corresponds to a transformation of the three (stator) coils into two equivalent coils with the same considerations or aspects in terms of flux f. m. m. torque or at least an image that will be perfectly proportional to them [26-27].

From the reference frame of the figure (III.7), we add another reference frame, characterized by a system of axes (d q) rotating at speed $w_s = \frac{d\theta_s}{dt}$ this frame is often referred to as the Park frame Figure (III.8). We can define a transition matrix from the $(\alpha, \beta, 0)$ frame to the $(d, q, 0)$ frame, defined as follows:

$$\begin{bmatrix} X_d \\ X_q \\ X_0 \end{bmatrix} = \begin{bmatrix} cos\theta & \sin\theta & 0 \\ -sin\theta & \cos\theta & 0 \\ 0 & 0 & 1 \end{bmatrix} \begin{bmatrix} X_\alpha \\ X_\beta \\ X_0 \end{bmatrix} \qquad \text{(III.30)}$$

Park's transformation is the unique transformation allowing the direct passage from the three-phase system to the rotating two-phase system, this transformation noted [P], it is defined by:

$$\left[P\ (\theta)\right] = \sqrt{\frac{2}{3}} \begin{bmatrix} \cos(\theta) & \cos(\theta - \frac{2\pi}{3}) & \cos(\theta - \frac{4\pi}{3}) \\ -\sin(\theta) & -\sin(\theta - \frac{2\pi}{3}) & -\sin(\theta - \frac{4\pi}{3}) \\ \frac{1}{\sqrt{2}} & \frac{1}{\sqrt{2}} & \frac{1}{\sqrt{2}} \end{bmatrix} \qquad \text{(III.31)}$$

In the same way, we define the inverse matrix $[P]^{-1}$to switch from two-phase to three-phase reference.

$$[P]^{(-1)} = \sqrt{\frac{2}{3}} \begin{bmatrix} \cos\theta & -\sin\theta & \frac{1}{\sqrt{2}} \\ \cos(\theta - \frac{2\pi}{3}) & -\sin(\theta - \frac{2\pi}{3}) & \frac{1}{\sqrt{2}} \\ \cos(\theta - \frac{4\pi}{3}) & -\sin(\theta - \frac{4\pi}{3}) & \frac{1}{\sqrt{2}} \end{bmatrix} \quad \text{(III.32)}$$

Note that $P^{(-1)} = P^{(-T)}$, so this transformation is orthogonal. The transition from variables $X_{a,b,c}$ to variables $X_{d,q}$ and vice versa is written in the following matrix form:

$$\begin{bmatrix} X_d \\ X_q \\ X_0 \end{bmatrix} = \left[P(\theta)\right] \begin{bmatrix} X_a \\ X_b \\ X_c \end{bmatrix} \quad \text{(III.33)}$$

$$\begin{bmatrix} X_a \\ X_b \\ X_c \end{bmatrix} = [P(\theta)]^{-1} \begin{bmatrix} X_d \\ X_q \\ X_0 \end{bmatrix} \quad \text{(III.34)}$$

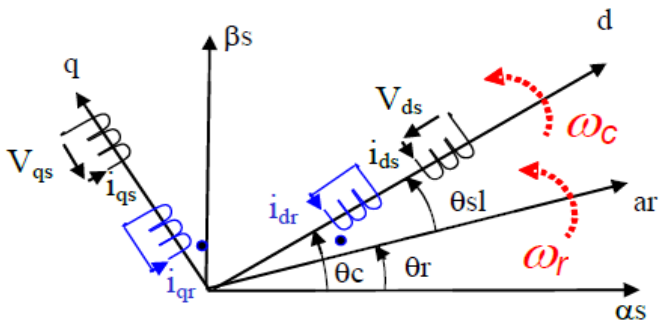


Figure (III.8): Diagram of the IM in Park's reference frame.

Or:

- $\theta s1$ Angle between rotor phase axis "ar" and the direct (d) axis.
- θc Angle between stator phase axis "as" and the direct (d) axis.
- θr Angle between the stator phase "as" and the rotor phase "ar".
- ωr Electrical angular speed of the rotor.
- ωc Angular speed of the rotating reference frame (Park's frame).

III.5.4 Application of the Park transformation:

The general voltage equations are obtained by writing Faraday's law for each of the stator and rotor windings [25]:

$$\begin{cases} V_{ds} = R_s I_{ds} + \dfrac{d}{dt}\phi_{ds} - w_s \phi_{qs} \\ V_{qs} = R_s I_{qs} + \dfrac{d}{dt}\phi_{qs} + w_s \phi_{ds} \\ V_{dr} = 0 = R_r I_{dr} + \dfrac{d}{dt}\phi_{dr} - (w_s - w_r)\phi_{qr} \\ V_{qr} = 0 = R_r I_{qr} + \dfrac{d}{dt}\phi_{qr} + (w_s - w_r)\phi_{dr} \end{cases} \quad \text{(III.35)}$$

With:

w_s : Angular velocity of the two-phase reference frame. The flow equations are given by:

$$\begin{cases} \phi_{ds} = L_s I_{ds} + L_m I_{dr} \\ \phi_{qs} = L_s I_{qs} + L_m I_{qr} \\ \phi_{dr} = L_r I_{dr} + L_m I_{ds} \\ \phi_{qr} = L_r I_{qr} + L_m I_{qs} \end{cases} \quad \text{(III.36)}$$

$$T_{em} = pL_m (I_{dr} I_{qs} - I_{qr} I_{ds}) \quad \text{(III.37)}$$

III.5.5 Choice of reference system:

There are three reference systems [28]

- Reference frame linked to stator axis (α, β) when $(w_s = 0)$,
- Reference frame linked to rotor axis (x, y) when $(w_s = w_r)$,
- Reference frame linked to rotating field of axis (d, q) when $(w_{s1} = w_s - w_r) = g w_s$.

III.6 Model of the asynchronous machine in the (d,q) frame of reference:

The model of the asynchronous machine in the (d,q) frame, after transformation, is given by [29]

$$\begin{cases} \dfrac{d}{dt}I_{ds} = \dfrac{1}{\sigma L_s}\left[-\left(R_S + \dfrac{L_m^2}{L_r T_{ro}}\right)I_{ds} + w_s \sigma L_s I_{qs} + \dfrac{L_m}{L_r T_{ro}}\phi_{dr} + \dfrac{L_m}{L_r} w_r \phi_{qr} + V_{ds}\right] \\ \dfrac{d}{dt}I_{qs} = \dfrac{1}{\sigma L_s}\left[-w_s \sigma L_s I_{ds} - \left(R_S + \dfrac{L_m^2}{L_r T_{ro}}\right)I_{qs} - \dfrac{L_m}{L_r} w_r \phi_{dr} + \dfrac{L_m}{L_r T_{ro}}\phi_{dr} + V_{qs}\right] \\ \dfrac{d}{dt}\phi_{dr} = \dfrac{L_m}{T_{ro}} I_{ds} - \dfrac{1}{T_{ro}}\phi_{dr} + (w_s - w_r)\phi_{qr} \\ \dfrac{d}{dt}\phi_{qr} = \dfrac{L_m}{T_{ro}} I_{qs} - (w_s - w_r)\phi_{dr} - \dfrac{1}{T_{ro}}\phi_{qr} \\ \dfrac{d}{dt}\Omega_r = \dfrac{1}{J}\left[p\,\dfrac{L_m}{L_r}\left(\phi_{dr} I_{qs} - \phi_{qr} I_{ds}\right) - T_r - f_c \Omega_r\right] \end{cases} \quad \text{(III.38)}$$

Or:

$\sigma = 1 - \dfrac{L_m^2}{L_s L_r}$ Dispersion coefficient

$T_{ro} = \dfrac{L_r}{R_r}$ Rotor time constant.

The equations of electromagnetic torque and motion are given by the following expressions:

$$T_{em} = p\left(\varphi_{ds} i_{dq} - \varphi_{dq} i_{ds}\right) \quad \text{(III.39)}$$

$$J\,\frac{d\,\Omega}{dt} = T_{em} - T_r - f_c.\Omega \quad \text{(III.40)}$$

III.7 Modeling of the voltage inverter:

The conversion of DC to AC energy through static power converters, such as voltage inverters, is a fundamental function within the expanding domain of power electronics. These converters are utilized in a wide array of applications, with prominent examples including variable-speed AC motor drives and uninterruptible power supplies (UPS).

A typical inverter topology consists of six bidirectional switches, each comprising a transistor and an anti-parallel recovery diode. These switches are arranged in pairs designated as S_a, S_b, S_c and are operated in a complementary manner. This control strategy ensures continuous current flow through the stator windings of the machine while simultaneously preventing short circuits across the DC power source.

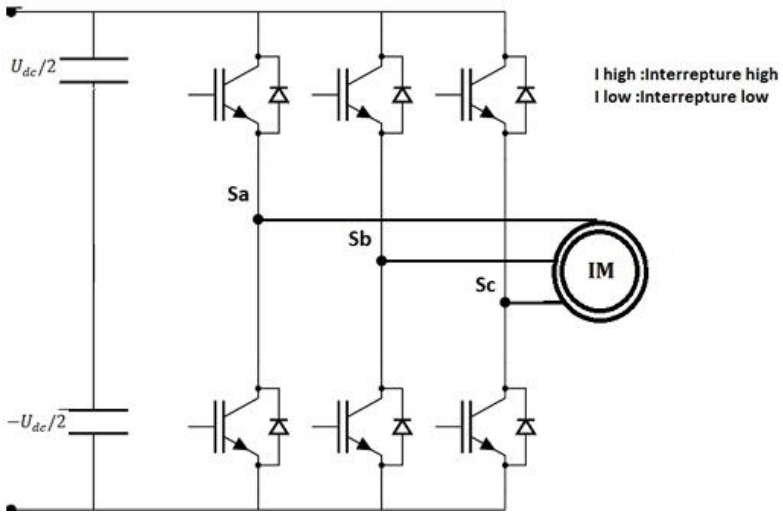


Figure (III.9): Representation of the two-level inverter feeding an IM.

III.7.1 Voltages in the phases of the induction machine:

To simplify the study, it is assumed that switching of the switches is instantaneous and that voltage drops across the switches are negligible. Compound voltages are given by:

$$\begin{cases} U_{AB} = V_{ao} - V_{bo} \\ U_{BC} = V_{bo} - V_{co} \\ U_{CA} = V_{co} - V_{ao} \end{cases} \quad \text{(III.41)}$$

V_{ao}, V_{bo}, V_{co} Are the inverter output voltages relative to reference 'o', the phase voltages are given by:

$$\begin{cases} U_{as} = V_{ao} - V_{no} \\ U_{bs} = V_{bo} - V_{no} \\ U_{cs} = V_{co} - V_{no} \end{cases} \quad \text{(III.42)}$$

V_{no} Is the load neutral voltage with respect to point " o ". We have: $V_{as} + V_{bs} + V_{cs} = 0$

$$V_{no} = \frac{1}{3}(V_{ao} + V_{bo} + V_{co}) \tag{III.43}$$

Replacing (III.43) in (III.42) gives:

$$\begin{cases} V_{as} = \frac{2}{3}V_{ao} + \frac{1}{3}V_{bo} + \frac{1}{3}V_{co} \\ V_{bs} = \frac{1}{3}V_{ao} + \frac{2}{3}V_{bo} + \frac{1}{3}V_{co} \\ V_{as} = \frac{1}{3}V_{ao} + \frac{1}{3}V_{bo} + \frac{2}{3}V_{co} \end{cases} \tag{III.44}$$

Matrix form:

$$\begin{bmatrix} V_{an} \\ V_{bn} \\ V_{cn} \end{bmatrix} = \frac{1}{3}U_{dc} \begin{pmatrix} 2 & -1 & -1 \\ -1 & 2 & -1 \\ -1 & -1 & -1 \end{pmatrix} \begin{pmatrix} S_a \\ S_b \\ S_c \end{pmatrix} \tag{III.45}$$

III.8 Simulation Results and Analysis:

- **Torque Response:** Highlights the machine's ability to maintain torque under dynamic loads.
- **Speed Response:** Demonstrates smooth acceleration and deceleration.
- **Flux Trajectory:** Validates the control strategy by showing a consistent flux pattern in the $\alpha - \beta$ plane

The simulation presented in Figures (III.10) and (III.11) illustrates the dynamic behavior of an induction motor (IM) under two different control strategies: without PWM (conventional supply) and with PWM voltage control.

In Figure (III.10), without PWM, the rotor speed gradually reaches its steady-state value, but with noticeable oscillations and a relatively slower transient response. The torque response exhibits considerable ripple during startup, and the stator current waveform is distorted with visible noise, indicating the presence of harmonics.

In Figure (III.11), although the PWM control is applied, we observe a similar dynamic trend with no substantial enhancement. In fact, more pronounced ripples appear in the torque and current signals, suggesting that PWM alone does not sufficiently improve control performance in this configuration. This highlights the limitations of basic PWM and motivates the use of more advanced control strategies for better torque regulation and current quality.

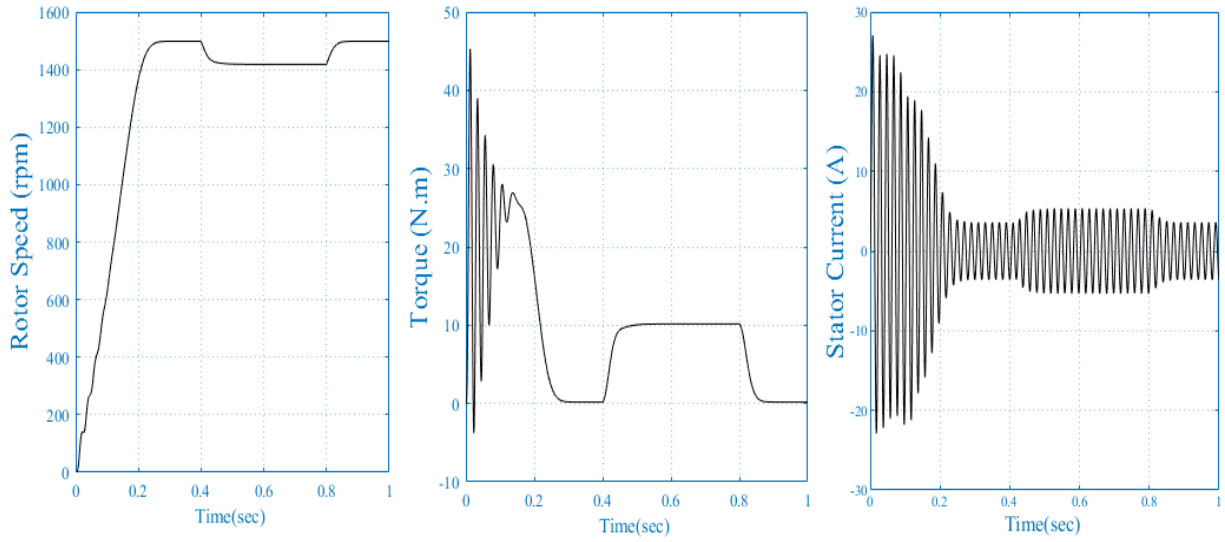


Figure (III.10): Simulation results of an induction machine without PWM

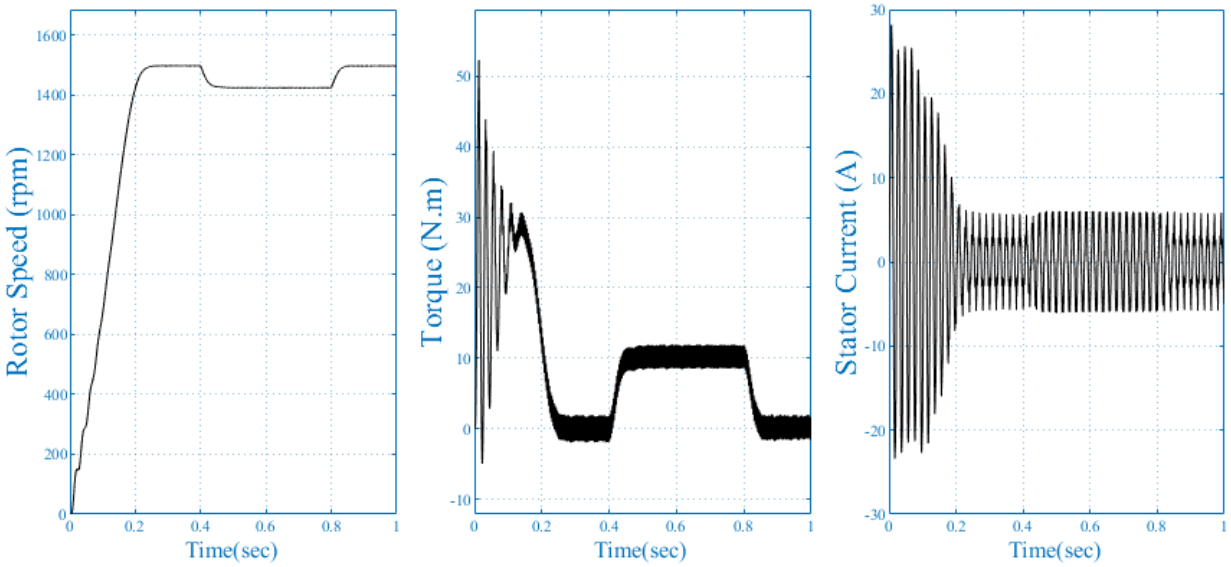


Figure (III.11): Simulation results of an induction machine with PWM.

III.9 Conclusion

In this chapter, a comprehensive study of the asynchronous (induction) machine was presented, covering both its theoretical modeling and dynamic simulation. The chapter began with an overview of the structural components of the induction motor, including the stator and rotor, along with the principle of electromagnetic induction which governs its operation. The mathematical modeling was developed in the $d-q$ (direct-quadrature) reference frame, providing a clear description of the electromechanical behavior and enabling advanced control strategies.

The simulation results compared two cases: an open-loop and a closed-loop control of the induction machine. Both scenarios showed relatively similar behavior in terms of rotor speed evolution and torque response. However, the closed-loop control exhibited slightly improved stability in torque tracking and smoother speed convergence. Minor torque ripples and current oscillations were still observed, indicating that while control improved performance, it did not fully eliminate disturbances. These results underline the importance of control strategy tuning and confirm that basic feedback can enhance performance.

Overall, this chapter successfully established the foundation for understanding, analyzing, and simulating induction machines under various operating conditions. It also confirmed the effectiveness of PWM control in improving dynamic response and operational reliability, which is crucial for high-performance industrial applications.

Chapter IV:

Direct torque control of induction machine

IV.1 Introduction:

The direct torque control (DTC) technique for asynchronous machines was introduced by Japanese and German researchers M. TAKAHACHI and I. DEPENBORK in 1985. Direct torque control methods consist of directly controlling the closing or opening of inverter switches from pre-calculated stator flux and torque values [30].

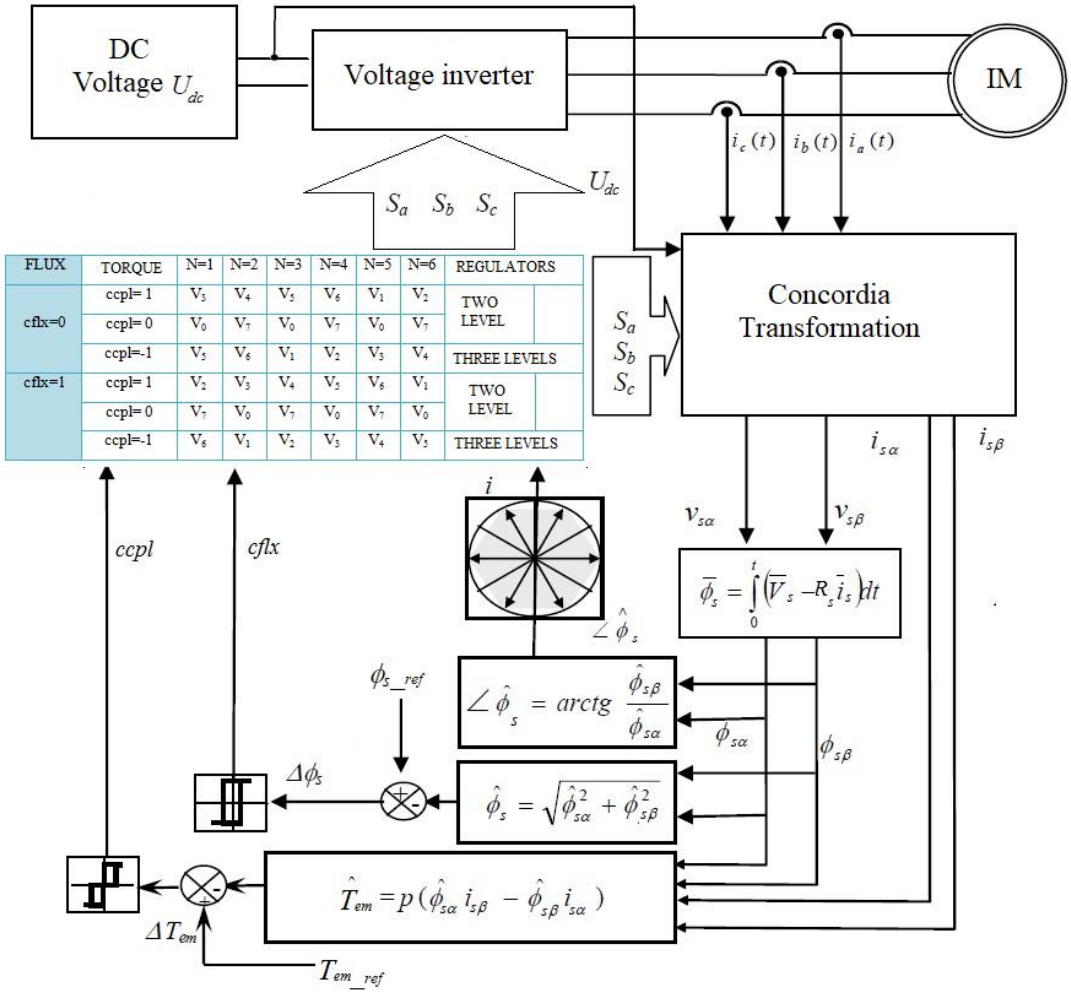
In this chapter, we present the core principles of Direct Torque Control (DTC). Then we describe the estimation techniques used for the two key variables stator flux and electromagnetic torque. Finally, we analyze simulation results to assess the performance and effectiveness of the control strategy.

IV.2 The principle of direct torque control:

The principle of direct torque control (DTC) is based on the estimation of the stator flux, using the instantaneous values of the voltage vector V_s. A three-phase inverter can provide eight instantaneous base voltage vectors, two of which are zero.

These vectors are chosen from a commutation table based on the flux and torque errors and the position of the stator flux vector. In this technique, the rotor position is no longer needed to choose the voltage vector, this feature defines DTC as a well-suited method for sensor-less control of AC machines [31]. Based on real-time measurements of the DC-link voltage at the inverter input and the stator phase currents, the model continuously estimates:

- The instantaneous stator flux vector ϕ_s
- The electromagnetic torque T_{em} generated by the motor
- The angular position or sector of the stator flux vector



FLUX	TORQUE	N=1	N=2	N=3	N=4	N=5	N=6	REGULATORS
cflx=0	ccpl= 1	V_3	V_4	V_5	V_6	V_1	V_2	TWO LEVEL
	ccpl= 0	V_0	V_7	V_0	V_7	V_0	V_7	
	ccpl=-1	V_5	V_6	V_1	V_2	V_3	V_4	THREE LEVELS
cflx=1	ccpl= 1	V_2	V_3	V_4	V_5	V_6	V_1	TWO LEVEL
	ccpl= 0	V_7	V_0	V_7	V_0	V_7	V_0	
	ccpl=-1	V_6	V_1	V_2	V_3	V_4	V_5	THREE LEVELS

Figure (IV.1): General block diagram of DTC controlled Induction Motor

IV.2.1 Operation of a Three-Phase Voltage Inverter

The switches of the voltage inverter (Figure IV.2) must be controlled in a way that maintains the machine's flux and torque.

The stator voltage vector V_s can be expressed as

$$\overline{V_s} = \sqrt{\frac{2}{3}} U_{dc} \left[S_a + S_b e^{j\frac{2\pi}{3}} + S_c e^{j\frac{4\pi}{3}} \right] \qquad (IV.1)$$

Where (s_a, s_b, s_c) represent the logical states of the three switches: $s_i = 1$ means the upper switch is closed and the lower switch is open ($V_i = +\frac{U_{dc}}{2}$), and $s_i = 0$ means the upper switch is open and the lower switch is closed ($V_i = -\frac{U_{dc}}{2}$).

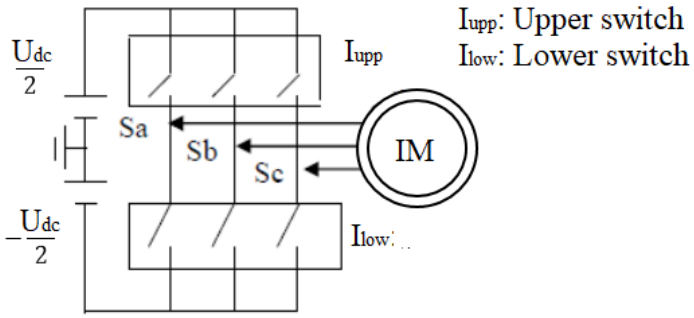


Figure (IV.2): Asynchronous Machine Controlled by a Voltage Inverter

The objective is to control the flux and torque by selecting an appropriate voltage vector through the configuration of the inverter switches. Since there are three switches, there are 2^3=8 possible combinations for the voltage vector V_s .

Two vectors, V_0 and V_7, correspond to the zero vector: (s_a, s_b, s_c)=(0,0,0) and (s_a, s_b, s_c)=(1,1,1).

- $V_0(0,0,0)$ Is always adjacent to an odd-numbered vector: $V_1(1,0,0)$, $V_3(0,1,0)$, or $V_5(0,0,1)$ allowing for only a single switching action.
- $V_7(1,1,1)$ Is always adjacent to an even-numbered vector: $V_2(1,1,0)$, $V_4(0,1,1)$ or $V_6(1,0,1)$,again resulting in only one switching.

During each modulation period, one inverter leg does not switch twice.

Figure (IV.3) shows the representation in the complex plane of the six non-zero voltage vectors that can be generated by a two-level three-phase voltage inverter. The process is as follows:

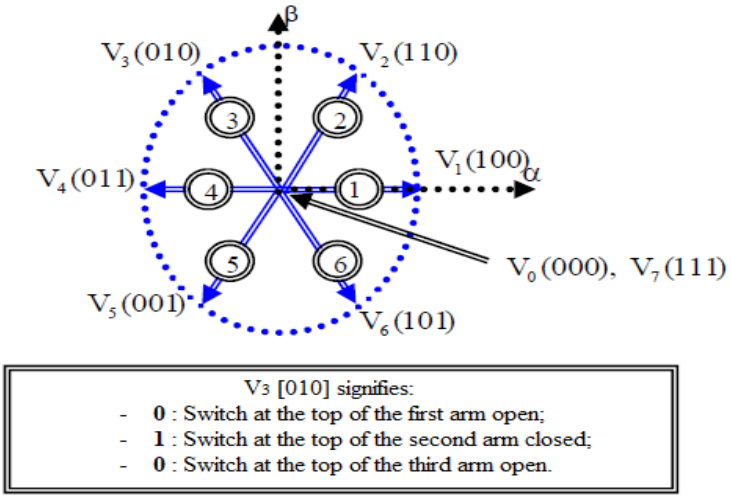


Figure (IV.3): Operating Sequences of a Two-Level Voltage Inverter

IV.2.2 Stator flux and electromagnetic torque control

IV.2.2.1 Stator flux control

In the frame linked to the stator of the machine, the stator flux can be obtained by the following equation [31]:

$$\overline{\phi_s} = \int_0^t (\overline{V_s} - R_s.\overline{I_s})dt + \phi_{so} \qquad \text{(IV.2)}$$

When a non-zero voltage vector is applied, the term $\overline{Rs}\,\overline{Is}$ since $Vs \gg Rs$ is over the time interval $[0,\ T_{ec}]$. As a result, equation (IV.2) can be simplified as follows:

$$\phi_s(t) = \phi_{s0} + V_s T_{ec} \qquad \text{(IV.3)}$$

$$\Delta\phi_s = \phi_s - \phi_{s0} = V_s T_{ec} \qquad \text{(IV.4)}$$

ϕ_{s0} Is the flux vector at time t=0.

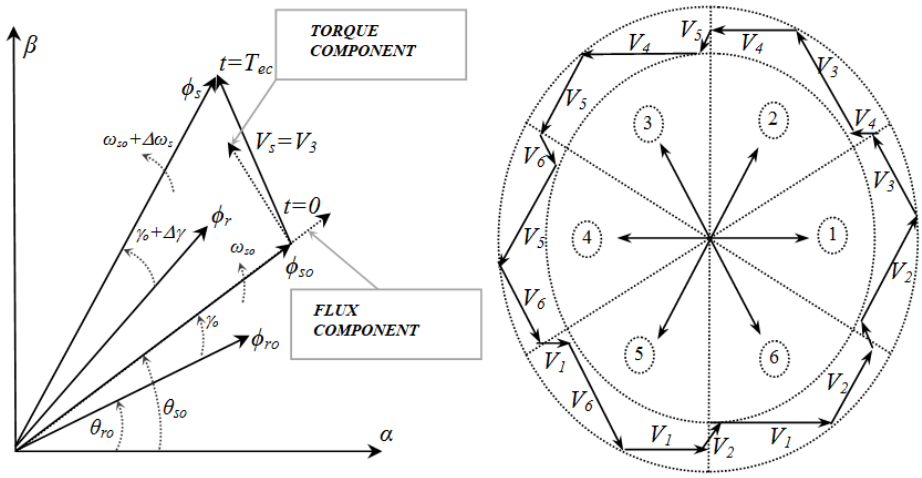


Figure (IV.4): Evolution of the end of vector ϕ_s for negligible R_sI_s.

Figure (IV.4) represents the evolution of the end of ϕ_s for negligible $R_s.I_s$, we note that the end of the stator flux vector moves on a straight line whose direction is given by the applied voltage vector V_s. Figure (IV.4) illustrates this principle, for example, when the vector $V_s = V_3$ is selected

The radial component (flux component) of the voltage vector acts on the amplitude of the flux vector ϕ_s and its tangential component (torque component) on the position of the flux vector ϕ_s [33].

By choosing the correct sequence of voltage vectors V_s, we can force the end of the flux vector ϕ_s to follow a desired trajectory. To operate with a virtually constant modulus ϕ_s, it's sufficient to choose an almost circular trajectory for the end of the flux vector. If the time interval T_{ec}, is very small compared to the period of rotation of the stator flux. The direction of motion of the stator flux vector ϕ_s is determined by its derivative, since the applied voltage vector V_s is non-zero.

The term $R_s.I_s$ is neglected, so ($V_s = \frac{ds}{dt}$). The speed of rotation of ϕ_s depends strongly on the choice of V_s, it is maximum for a vector V_s perpendicular to the direction of ϕ_s, and zero if a zero vector is applied. It can also be negative [31].

IV.2.2.2 Electromagnetic torque control:

The vector expressions of the IM in the reference frame linked to the stator are given by [31].

$$\vec{V}_s = R_s \vec{I}_s + \frac{d\vec{\phi}_s}{dt}$$
$$\vec{V}_r = 0 = R_r \vec{I}_r + \frac{d\vec{\phi}_r}{dt} - j\sigma\vec{\phi}_r \quad \text{(IV.5)}$$

$$\vec{\phi}_s = L_s \vec{I}_s + L_m \vec{I}_r$$
$$\vec{\phi}_r = L_r \vec{I}_r + L_m \vec{I}_s \quad \text{(IV.6)}$$

From the flux expressions, the rotor current is written

$$\vec{I}_r = \frac{1}{\sigma L_r}\left(\frac{L_m}{L_r}\vec{\phi}_s - \vec{\phi}_r\right) \quad \text{(IV.7)}$$

The equations for stator voltage and rotor flux are written:

$$\vec{V}_s = R_s \vec{I}_s + \frac{d\vec{\phi}_s}{dt} \quad \text{(IV.8)}$$

$$\frac{d\vec{\phi}_r}{dt} + (1 - j\omega)\vec{\phi}_r = \frac{L_m}{L_r} \cdot \frac{d\vec{\phi}_s}{dt} \quad \text{(IV.9)}$$

In addition $\overline{\phi}_r$ reached in steady state:

$$\vec{\phi}_r = \frac{L_m}{1 + j\omega_r \sigma}\vec{\phi}_s \quad \text{(IV.10)}$$

The Torque is expressed by:

$$T_{em} = p \cdot \frac{L_m}{\sigma L_r} \cdot \left\|\vec{\phi}_s\right\| \cdot \left\|\vec{\phi}_r\right\| \cdot \sin\gamma \quad \text{(IV.11)}$$

The electromagnetic torque depends on the magnitudes of the stator and rotor flux vectors, ϕ_s and ϕ_r well as their relative position. If the stator flux ϕ_s is perfectly controlled based on the

magnitude and orientation of the voltage vector $\overline{V_s}$ then both the amplitude and the relative position of ϕ_r can also be regulated, allowing precise control of the torque.

However, this is only achievable if the switching period is significantly smaller than the rotor time constant.

IV.2.3 Choice of the voltage vector $\overline{V_s}$:

To fix the amplitude of the stator flux, the end of the flux vector must have a circular trajectory, the applied voltage vector must always be perpendicular to the flux vector, but since we have eight desired fixed vectors. This is achieved by hysteresis comparators, for the flux and the torque. The choice of V_s then depends on the desired variation for the stator flux module, and the direction of rotation, but also on the desired evolution for the torque [34].

In this way, we define the evolutionary space of ϕ_s in the stator frame of reference by decomposing it into six zones N = i, with i=1... 6, [34]

The choice of the vector V_s depends:

- on the position of ϕ_s
- on the desired variation in the magnitude of ϕ_s
- on the desired variation in torque.
- of the direction of rotation of ϕ_s

When the flux is in a zone i, flux and torque control can be ensured by selecting one of the following eight voltage vectors [16-17]:

- If $\overline{V}_{i+1}(V_2)$ is selected then ϕ_s increases and T_{em} increases.
- If $\overline{V}_{i+1}(V_6)$ is selected thenϕ_s increases and T_{em} decreases.
- If $\overline{V}_{i+2}(V_3)$ is selected then $\phi_s$decreases and T_{em} increases.
- If $\overline{V}_{i-2}(V_5)$ is selected then $\phi_s$decreases and T_{em} decreases.

If V_0 or V_7 are selected, then flux $\overline{\phi}_s$ rotation is stopped, resulting in a decrease in torque while flux modulus $\overline{\phi}_s$remains unchanged.

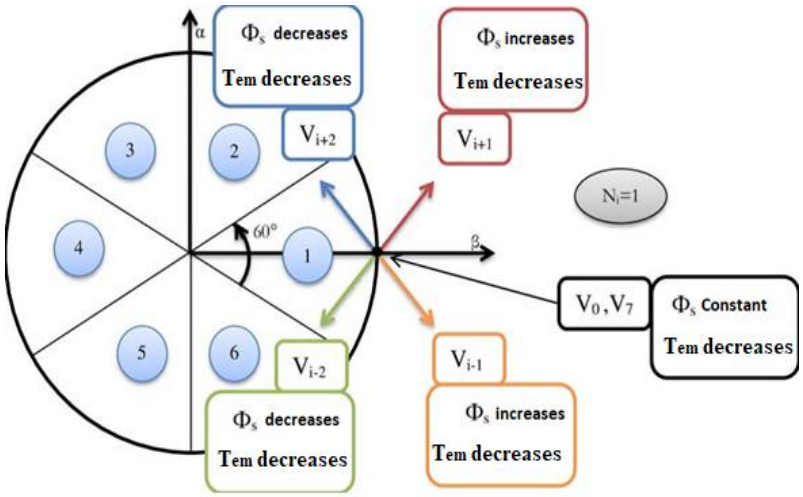


Figure (IV.5): Choice of voltage vector [34].

Figure (IV.6) highlights the impact of changing the voltage vector depending on the position of the flux vector within Zone I. At the start of the zone, the vectors v_{i+1} and v_{i-2} are nearly aligned with the flux vector. As a result, their influence on the flux is minimal, they do not significantly alter the torque, and the flux remains relatively unchanged. In the same position, the angles between v_{i-1} or v_{i+2} and the flux vector are approximately 150° and 30°, respectively. These vectors produce a small torque component and have limited impact on the flux. However, when these vectors are applied, noticeable variations in the flux occur, and the resulting torque changes become more significant.

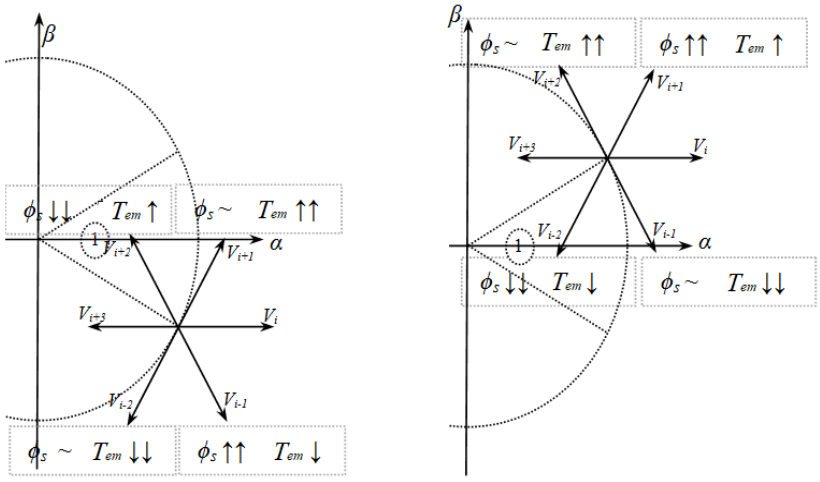


Figure (IV.6): No significant change

IV.3 Estimators:

The estimator, obtained by integrating the stator voltages in the fixed axes (α, β) ,has been widely used for DTC. Due to its simplicity, this structure has significant limitations. The main drawback is operation at low speeds, due to its sensitivity to variations in resistance R_s during operation [38].

IV.3.1 Estimation of the stator flux:

The estimation of the flux can be carried out from the measurements of the stator current and voltage quantities of the machine, the expression of the stator flux is written [32-33]:

$$\phi_s = \int_0^t (\overline{V_s} - R_s \overline{I_s}) dt \tag{IV.12}$$

We obtain the components α and β of the vector:

$$\overline{\phi_s} = \phi_{s\alpha} + j\phi_{s\beta} \tag{IV.13}$$

$$\begin{cases} \phi_{s\alpha} = \int_0^t \left(V_{s\alpha} - R_s I_{s\beta} \right) dt \\ \phi_{s\beta} = \int_0^t \left(V_{s\beta} - R_s I_{s\alpha} \right) dt \end{cases} \tag{IV.14}$$

We obtain the voltages $V_{s\alpha}$ and $V_{s\beta}$, from commands (S_1, S_2, S_3) , and the DC bus voltage U_{dc}

$$\overline{V_s} = V_{s\alpha} + jV_{s\beta} \tag{IV.15}$$

$$\begin{cases} V_{s\alpha} = \sqrt{\frac{2}{3}} U_{dc} \left[S_a - \frac{1}{2}(S_b + S_c) \right] \\ V_{s\beta} = \frac{1}{\sqrt{2}} U_{dc} (S_b - S_c) \end{cases} \tag{IV.16}$$

The modulus and phase of the stator flux are written:

$$|\phi_s| = \sqrt{\phi_{s\alpha}^2 + \phi_{s\beta}^2} \tag{IV.17}$$

$$\theta_s = \operatorname{arctg} \frac{\phi_{s\alpha}}{\phi_{s\beta}} \tag{IV.18}$$

This gives the currents $I_{S\alpha}$ and $I_{S\beta}$ are also obtained from the measurement of real currents I_{s1}, I_{s2} and $I_{s3}(I_{s1}+I_{s2}+I_{s3})=0$ and by applying the Concordia transformation:

$$\overline{I}_s = I_{s\alpha} + jI_{s\beta} \tag{IV.19}$$

$$\begin{cases} I_{s\alpha} = \sqrt{\frac{2}{3}} I_{sa} \\ I_{s\beta} = \frac{1}{\sqrt{2}}(I_{sb} - I_{sc}) \end{cases} \tag{IV.20}$$

IV.3.2 Estimation of the electromechanical torque:

The electromagnetic torque is estimated, only from the stator fluxes and currents in the frame (α,β) which can be put in the following form:

$$T_{em} = p\left[\phi_{s\alpha} I_{s\beta} - \phi_{s\beta} I_{s\alpha}\right] \tag{IV.21}$$

IV.4 Development of the control vector:

IV.4.1 Flux controller:

In order to obtain very good dynamic performances, the choice of a two-level hysteresis corrector (figure IV.7) seems to be the simplest and best suited solution for DTC control. With this type of regulator, one can easily control and maintain the end of the flux vector ϕ_s in a circular crown, as shown in figure IV.4 [36].

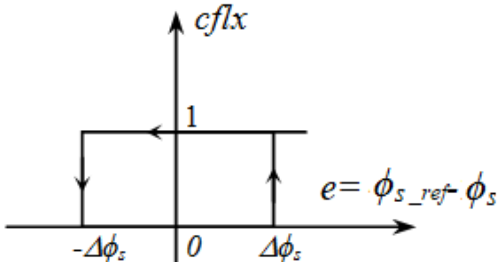


Figure (IV.7): Hysteresis flux corrector.

We can then write:

$$cflx = \begin{cases} 1 & \text{if } (\phi_s - \phi_s^*) > \Delta\phi \\ -1 & \text{if } (\phi_s - \phi_s^*) < -\Delta\phi \\ 0 & \text{if } |\phi_s - \phi_s^*| \leq \Delta\phi \end{cases} \tag{IV.22}$$

IV.4.2 electromagnetic torque controller:

The torque corrector is used to maintain the torque within the limits

$$\left| T_{em_ref} - T_{em} \right| \leq \Delta T_{em} \qquad \text{(IV.23)}$$

T_{em_ref}: is the reference torque.

ΔT_{em_ref}: is the corrector's hysteresis band.

However, the difference with flux control is that the torque can be positive or negative depending on the direction of rotation of the machine. Two solutions can be considered [34-35]:

a. a two-level hysteresis corrector,
b. a three-level hysteresis corrector.

IV.4.2.1 Two-level correctors:

This corrector is simpler to implement, and by correctly selecting zero vectors along the N_i zones, we can see that for each zone i, there is an inverter arm of the inverter that never switches, thus reducing the average switching frequency, thus reducing switching losses in the inverter. The model of two-level voltage inverter [38]

IV.4.2.2 Three-level correctors:

The three-level corrector allows the motor to be controlled in both directions of rotation, either for a positive torque ($ccpl = 1$), or for a negative torque ($ccpl = -1$) or decreased ($ccpl = 0$). It may be necessary to increase or decrease the electromagnetic torque of the machine but also to keep it constant [36].

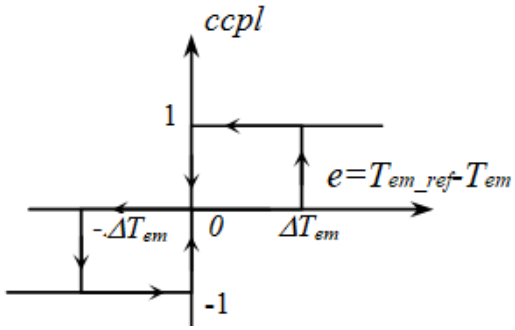


Figure (IV.8): Three level Torque corrector.

IV.4.3 Development of switching table:

Depending on the sector and the flux and torque evolution, we can choose the voltage vector V_s to be applied to respect the flux and torque set points. The switching table used to select the appropriate vector is based on the flux ($cflx$) and torque ($ccpl$) errors, and on the position of the stator flux vector (i=1… 6).

To control torque and stator flux, several commutation tables can be used, each of which has an influence on the behavior of the machine in terms of torque, stator flux, current ripple, switching frequency and the ability to operate in two or four quadrants of the torque-speed plane. In the following **Table** (IV.1), four tables switching are presented, while **Table** (IV.2) shows the table for the fourth most commonly used strategy [36], which is also proposed in our work.

Table (IV.1): Different strategies of switching tables [36].

	$T_{em} \uparrow \phi_s \uparrow$	$T_{em} \uparrow \phi_s \downarrow$	$T_{em} \downarrow \phi_s \uparrow$	$T_{em} \downarrow \phi_s \downarrow$
1^{st} *Strategy*	V_{i+1}	V_{i+2}	V_0, V_7	V_0, V_7
2^{nd} *Strategy*	V_{i+1}	V_{i+2}	V_i	V_0, V_7
3^{rd} *Strategy*	V_{i+1}	V_{i+2}	V_i	V_{i+3}
4^{th} *Strategy*	V_{i+1}	V_{i+2}	V_{i-1}	V_{i-2}

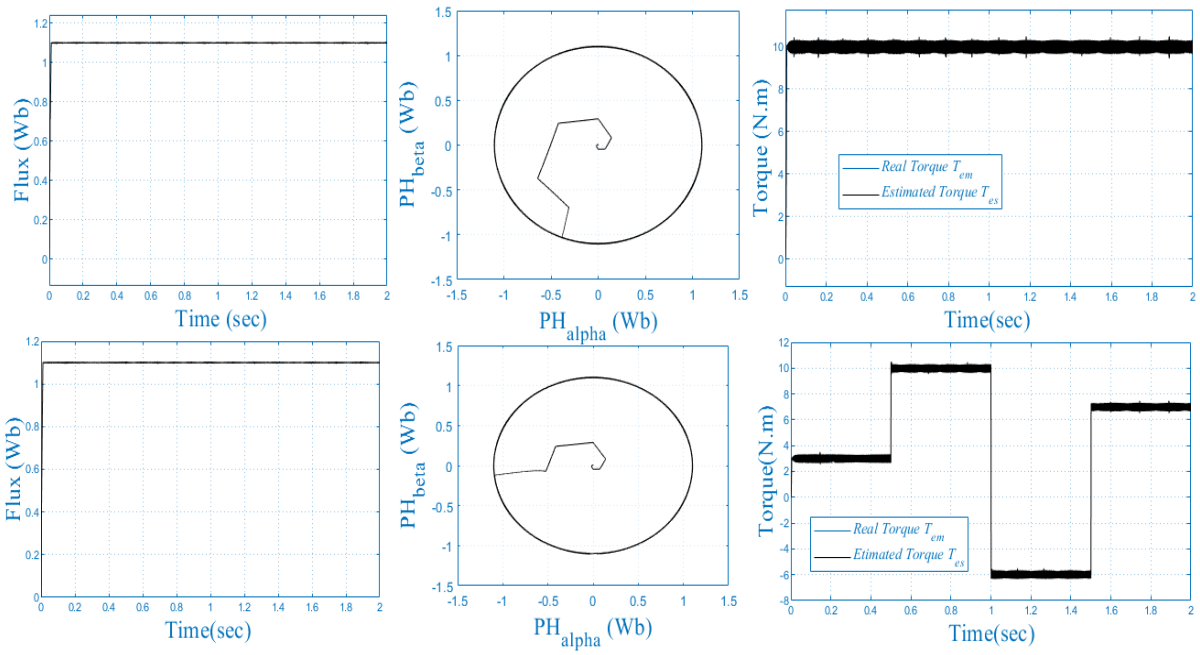
Table (IV.2): Control strategy with a two-level hysteresis comparator [18].

Flux	*Torque*	$N=1$	$N=2$	$N=3$	$N=4$	$N=5$	$N=6$	*Regulators*
$cflx=1$	$ccpl=1$	V_2	V_3	V_4	V_5	V_6	V_1	
	$ccpl=0$	V_7	V_0	V_7	V_0	V_7	V_0	
$cflx=0$	$ccpl=1$	V_3	V_4	V_5	V_6	V_1	V_2	*Two Level*
	$ccpl=0$	V_0	V_7	V_0	V_7	V_0	V_7	

IV.5 Simulation results for DTC of IM:

This section presents the simulation of Direct Torque Control applied to an induction motor with a torque set point of 10 (N·m) and a flux reference of 1.1 (Wb).

(A): Open-loop



(B): Closed-Loop

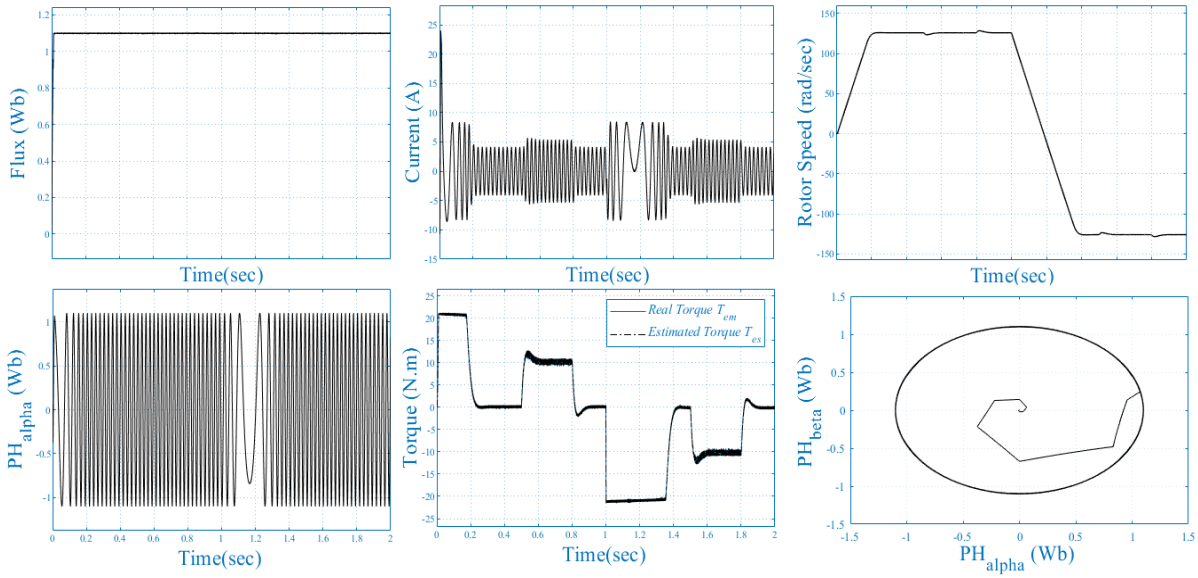


Figure (IV.9): Evolution of torque, stator flux and IM-DTC current [(A): open loop, (B): closed loop]

Two scenarios are shown: **Open-loop** and **Closed-loop** control. Each case includes six plots showing the evolution of stator flux, its trajectory in the $\alpha - \beta$ plane, and the torque response. The flux trajectory remains nearly circular, confirming stable control throughout the operation.

Figure (IV.9) illustrates the behavior of the induction motor under Direct Torque Control (DTC) in both open-loop and closed-loop configurations.

In the open-loop case (A), the flux trajectory in the α–β plane is relatively circular, Flux and the torque track their references. In contrast, the closed-loop case (B) demonstrates clear improvements, the flux is well-regulated, the current adapts to torque variation, and the rotor speed follows its reference even during reversals. The torque accurately tracks the reference, with real and estimated values matching closely. The α-β flux trajectory maintains its circular shape, confirming good flux control.

IV.6 Conclusion:

This chapter is devoted to the study of the Direct Torque Control (DTC) technique by examining its theoretical foundations, implementation methodology, and performance characteristics for induction machine drives. Through systematic analysis, we have demonstrated DTC's effectiveness as a high-performance control strategy that eliminates the need for mechanical sensors and complex transformations while maintaining robust torque dynamics.

Chapter V:

PV pumping system based on MPPT-Deep Learning

V.1 Introduction:

Artificial Neural Networks (ANN) has emerged as a powerful tool in solving complex nonlinear problems, particularly in the field of renewable energy. In Maximum Power Point Tracking (MPPT) applications, conventional methods such as Perturb and Observe (P&O) often suffer from oscillations around the Maximum Power Point (MPP) and slow tracking under rapidly changing atmospheric conditions.

To address these limitations, this chapter presents a Deep Multi-Layer Perceptron (Deep MLP)-based ANN approach for MPPT, which learns from historical data and generalizes patterns to improve tracking efficiency. This chapter also discuss the fundamental concepts of ANN, deep learning principles, the advantages of Deep MLP over conventional methods, and the training process using MATLAB and Simulink to achieve MPPT for PV panel connected initially to a DC load under varying irradiance and shading condition. To demonstrate the feasibility of the proposed MPPT-DNN algorithm, the DC load is later replaced by an AC load using pumping System.

V.2 Artificial intelligence (AI) overview:

Artificial Intelligence (AI) is rapidly emerging as one of the most transformative technologies of our time. Rather than relying solely on explicitly programmed rules, AI systems are designed to learn from data by identifying patterns and making informed decisions. This capability allows AI to perform complex tasks such as image recognition, speech processing, autonomous navigation, and decision-making areas that have traditionally required human intelligence.

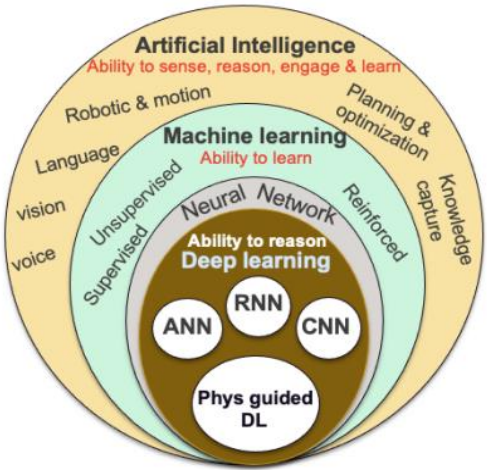


Figure (V.1): Diagram of AI.

V.3 Machine Learning Techniques:

Machine Learning (ML) is a subset of artificial intelligence (AI) that enables systems to automatically learn from data and improve their performance without being explicitly programmed. In engineering and energy systems, ML techniques are widely adopted to model complex, nonlinear relationships that are difficult to capture using traditional analytical methods.

V.3.1 Types of Machine Learning Techniques:

Machine learning can be categorized into several approaches depending on the nature of the data and the learning process. These approaches are essential to understand when selecting the appropriate method for a specific application. The figure below presents the main types of machine learning techniques.

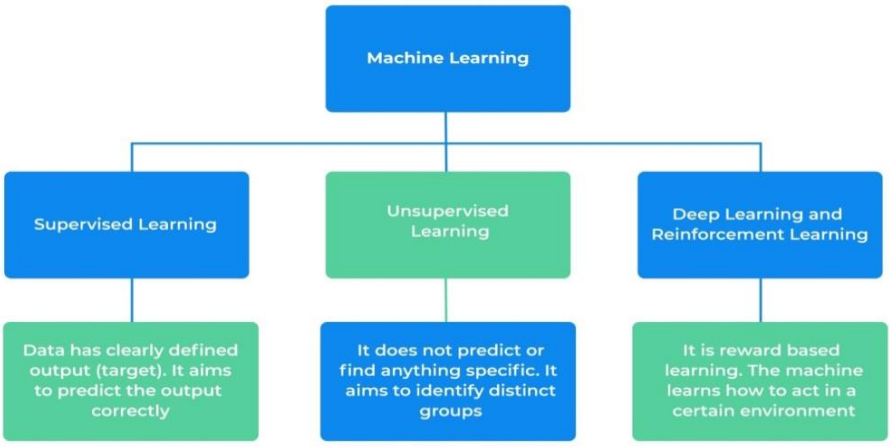


Figure (V-2): Machine Learning Techniques.

V.3.2 Supervised Learning:

Supervised learning is commonly used in PV systems to predict optimal operating points based on input variables such as solar irradiance; PV current; power and voltage, it requires labeled datasets containing both input features and corresponding output values.

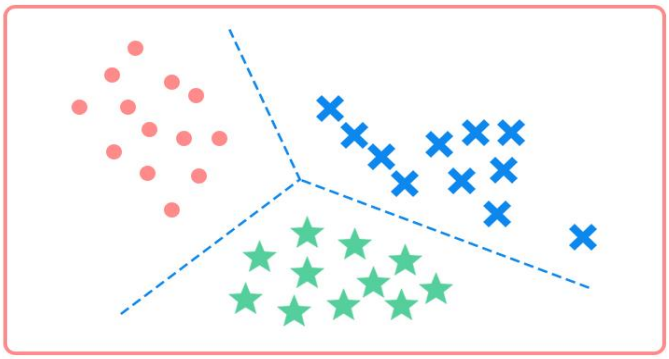


Figure (V-3): Supervised Learning**.**

V.3.3 Unsupervised Learning:

Identifies patterns without labeled outputs, Useful for fault detection or identifying operating states in solar PV systems.

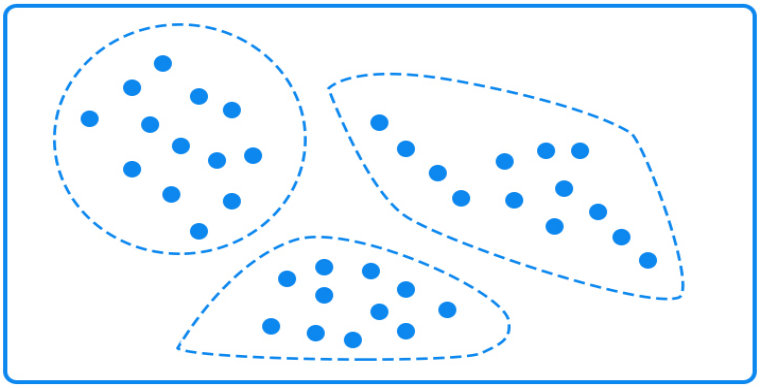


Figure (V-4): Unsupervised Learning.

V.3.4 Reinforcement Learning:

Optimizes decision-making using reward-based feedback, Emerging in MPPT techniques where the algorithm learns optimal control actions over time.

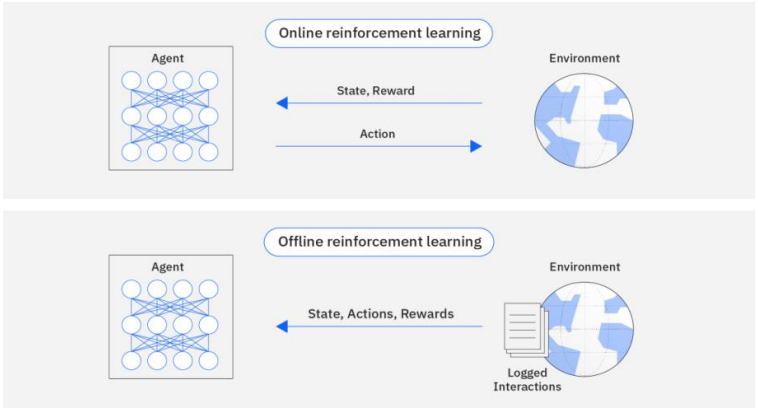


Figure (V-5): Reinforcement Learning.

V.4 Deep Learning Overview:

V.4.1 Definition and Principles:

Deep learning is a subset of machine learning that utilizes deep neural networks to model and process complex data. It mimics human cognitive functions by enabling machines to learn patterns and make decisions based on vast amounts of data. Deep learning is characterized by:

- Multiple hidden layers: Unlike traditional ANNs, deep learning architectures have many layers, enabling advanced feature extraction.

- Nonlinear transformations: Complex hierarchical representations of data.
- Optimization techniques: Stochastic gradient descent (SGD), Adam, and batch normalization improve learning efficiency.

Deep learning has revolutionized various fields, including image recognition, speech processing, and renewable energy applications. Deep learning outperforms traditional ANNs in handling nonlinear systems and large-scale data processing, making it ideal for solar MPPT optimization [39].

V.4.2 Multi-Layer Perceptron (MLP):

A Multi-Layer Perceptron (MLP) is a fully connected feedforward neural network consisting of an input layer, one or more hidden layers, and an output layer. It uses activation functions and is trained using backpropagation to learn complex patterns in data.

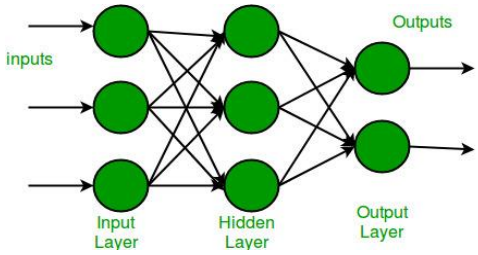


Figure (V-6): Multi-Layer Perceptron.

V.4.3 Convolutional Neural Networks (CNNs):

Specialized for image processing and spatial pattern recognition. CNNs use convolutional layers to automatically extract features from input images, making them highly effective in visual tasks such as object detection and classification. Pooling layers reduce dimensionality, improving computational efficiency. CNNs are widely used in applications such as medical imaging, facial recognition, and autonomous driving.

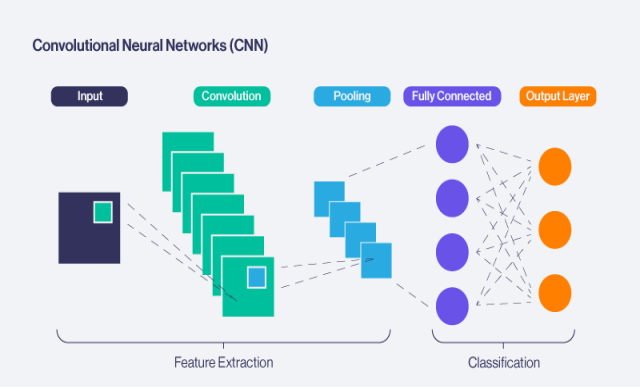


Figure (V-7): Convolutional Neural Networks.

V.4.4 Recurrent Neural Networks (RNNs):

Designed for sequential data, including Long Short-Term Memory (LSTM) networks. RNNs maintain internal memory through feedback connections, making them suitable for time-series analysis, language modeling, and other sequence prediction tasks. LSTMs address the vanishing gradient problem, enabling learning over long sequences. RNNs are commonly applied in speech recognition, machine translation, and text generation.

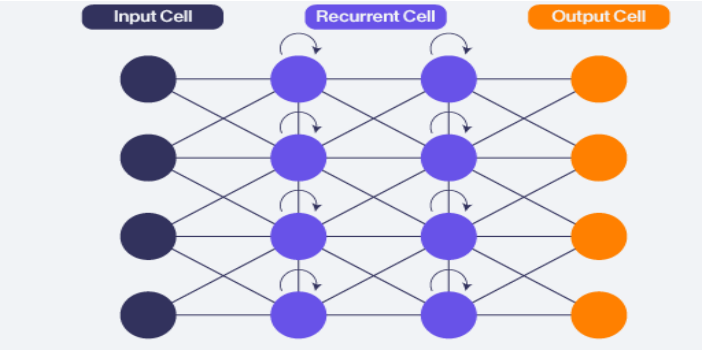


Figure (V-8): Recurrent Neural Networks.

V.4.5 Deep Reinforcement Learning:

Combines deep learning with decision-making frameworks, such as Deep Q-Networks (DQN).It enables agents to learn optimal actions through trial and error by interacting with an environment and receiving feedback in the form of rewards. Deep neural networks are used to approximate value functions or policies, allowing the agent to handle high-dimensional input spaces. Deep reinforcement learning has shown great success in fields like robotics, autonomous systems, and game-playing AI.

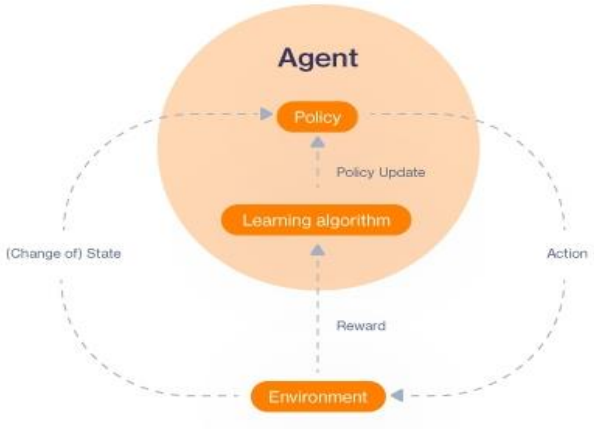


Figure (V-9): Deep Reinforcement Learning.

V.5 Artificial Neural Network:

A neural network or Artificial Neural Network is a computational model whose design is very schematically inspired by the functioning of real neurons.

Neural networks are generally optimized by statistical learning methods, so they are placed both in the family of statistical applications, which they enrich with a set of paradigms enabling the generation of vast, flexible and partially structured functional spaces, and in the family of artificial intelligence methods, which they enrich by enabling decisions to be made based more on perception than on formal logical reasoning.

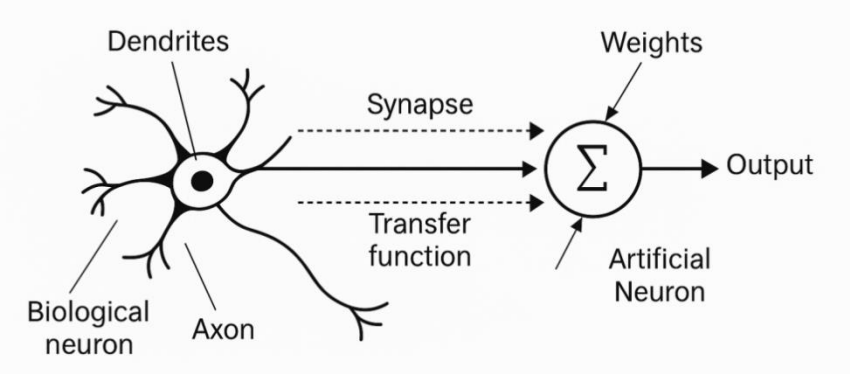


Figure (V-10): Comparison Between Biological Neuron and Artificial Neuron.

V.5.1 Neuron Input Computation:

Each neuron in the ANN receives multiple inputs, and the first step is to calculate the weighted sum of these inputs along with a bias term. This is given by:

$$a = \sum_{i=1}^{n} \omega_{ij} x_i + b_j \tag{V.1}$$

Here w_{ij} is the weight from the i^{th} input to the j^{th} neuron, x_i is the input signal, and b_j is the bias of the neuron j. This weighted summation is fundamental in ANNs and forms the basis for learning complex input-output relationships.[40]

V.5.2 Activation Function:

After calculating the weighted sum, an activation function $\phi(\cdot)$ is applied to introduce nonlinearity, enabling the network to learn complex mappings:

V.5.3 Output Computation:

For the output layer, the activations from the last hidden layer neurons are combined (usually linearly) to produce the network's output, which can represent quantities such as the optimal voltage or duty cycle for MPPT.

$$y_j = f\left(\sum_{i=1}^{n} \omega_{ij} x_i + b_j\right) \quad \text{(V.2)}$$

Where w_{ij} are the weights connecting the j^{th} hidden neuron to the output neuron, and b_j is the output bias [41].

V.6 Architectures of MLP Neural Network:

V.6.1. Shallow Neural Network (SNN):

A **shallow neural network** is a type of artificial neural network that contains only one hidden layer between the input and output layers. Despite its simplicity, it can approximate a wide range of functions, as proven by the universal approximation theorem. However, it often struggles with complex tasks that require deeper representations of data. [42].

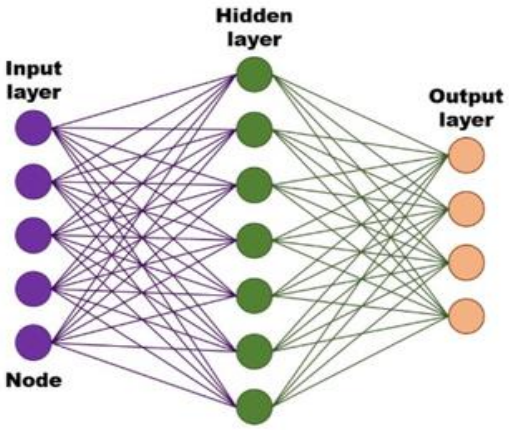


Figure (V-11): Schematic of shallow neural network.

V.6.2 Deep Neural Network (DNN):

A deep neural network is an artificial neural network with two or more hidden layers. These multiple layers enable the model to learn hierarchical representations of data, from low-level features to high-level abstractions, which is especially useful in fields like computer vision and natural language processing [43]

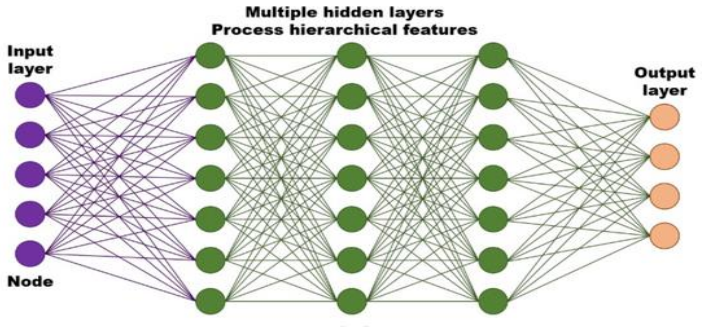


Figure (V-12): Schematic of Deep neural network

V.6.3 Difference between Shallow and Deep Neural Networks:

The primary difference between shallow and deep neural networks lies in depth shallow networks have a single hidden layer, while deep networks consist of multiple hidden layers.

This depth enables deep networks to learn more complex and abstract features, often outperforming shallow ones on tasks like image classification and language modeling. While shallow networks are easier and faster to train, they often require many more neurons to match the performance of deep networks on complex problems Deep networks, though more powerful, demand larger datasets, more computing power, and techniques like dropout and batch normalization to avoid over fitting.[44-45].

V.6 Artificial Neural Network based MPPT for Solar System:

V.6.1. Training procedure

Artificial Neural Network (ANN) based MPPT technique is used to receive the maximum power from solar PV system. The basic structure of ANN comprises three layers as an input layer, hidden layer and output layer. ANN is used to increase tracking speed and accuracy by modeling and forecasting a solar power system.

ANN based in MPPT technique is used as it gives accurate and fast response for different environmental conditions. Levenberg-Marquardt (trainlm) optimization algorithm, is used to train the neural network for MPPT of solar PV system which minimizes the Mean Squared Error (MSE) between predicted and actual values. The training data used for learning of the ANN based MPPT are gained from PV module. A flow chart of training procedure of ANN based MPPT for solar PV system has shown in Figure (V.13).

ANNs solve this by:

- Predicting the optimal duty cycle for DC-DC converters
- Using inputs such as PV voltage and current
- Learning the nonlinear relationship between environmental inputs and the MPP [46].

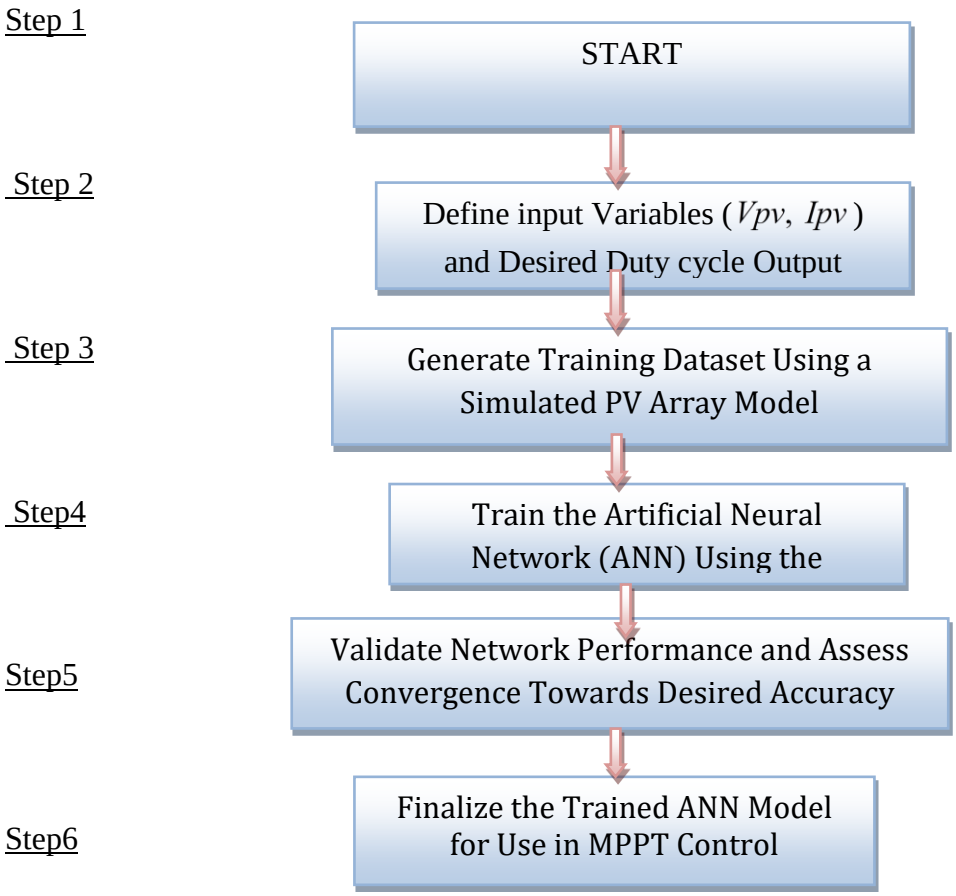


Figure (V.13): Training Procedure of ANN based MPPT for Solar PV System

V.6.2. ANN-MPPT Algorithm with DC load under irradiation variation

This section presents the simulation of an Artificial Neural Network (ANN)-based Maximum Power Point Tracking (MPPT) algorithm applied to a photovoltaic (PV) system connected to a resistive DC load. The main objective is to evaluate the tracking behavior of the ANN model under dynamic irradiance conditions using only one PV panel.

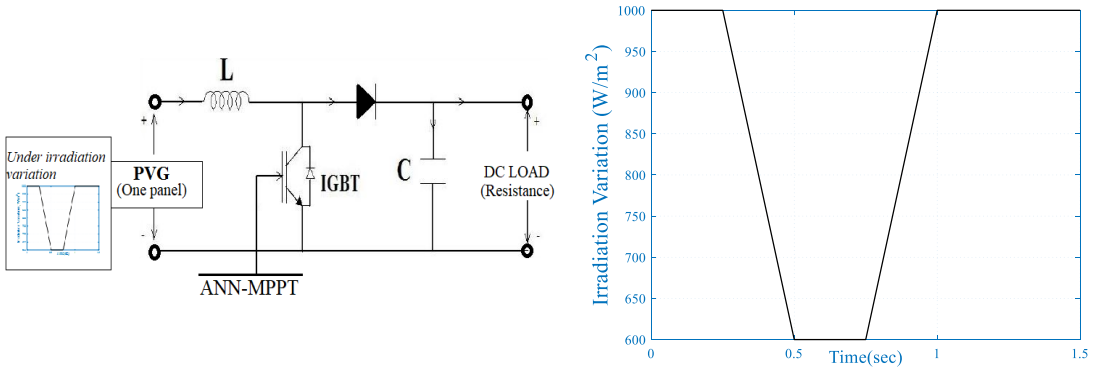


Figure (V-14): Temporal Variation of Solar Irradiance

This Figure (V-14) shows the temporal profile of solar irradiance used to simulate dynamic environmental conditions for the MPPT test. The irradiance begins at 1000 W/m² and decreases linearly to around 600 W/m² at 0.75 seconds, then rises back to 1000 W/m² by 1.5 seconds. This pattern replicates realistic scenarios such as passing clouds or environmental obstructions. The purpose of using such variation is to evaluate the responsiveness and adaptability of MPPT algorithms. In this case, an ANN-based MPPT controller is tested to determine how quickly it adjusts to changes and tracks the new maximum power point. Rapid and accurate adaptation is critical for minimizing power loss during shading. The slope and symmetry of the profile allow consistent analysis in both decreasing and increasing phases. This input scenario is essential for validating controller robustness in real-world solar energy systems where irradiance is rarely constant.

Two different neural network structures were implemented and tested: a shallow neural network (2-10-1) and a deep neural network (2-5-10-10-20-10-5-1). Both networks were trained using simulation data and evaluated based on their performance in adjusting the duty cycle to ensure maximum power output. The proposed models were trained with the Levenberg–Marquardt optimization algorithm, achieving convergence within 41 epochs for the shallow NN and 94 epochs for the deep NN. The training process met the early stopping criterion after 6 consecutive validation checks, a final validation mean squared error (MSE) reached was (4×10^{-5}) for SNN and (8.1×10^{-4}) for DNN, the first training procedure were conducted using Matlab 2018b.

The simulation results (Figure V-15) show PV output power and the duty cycle during varying irradiance conditions by applying MPPT-SNN and MPPT-DNN. The Deep NN (DNN) clearly demonstrates better performance, with faster convergence to maximum power and higher output throughout the test. In contrast, the Shallow NN (SNN) lags in adjusting to irradiance variation, especially during the drop and recovery phases, resulting in lower power extraction. The duty cycle response confirms this difference, the DNN provides smoother and more accurate adjustments to the control signal. So, according to this figure, we conclude that deeper architectures have better generalization and learning capacity, especially under dynamic conditions.

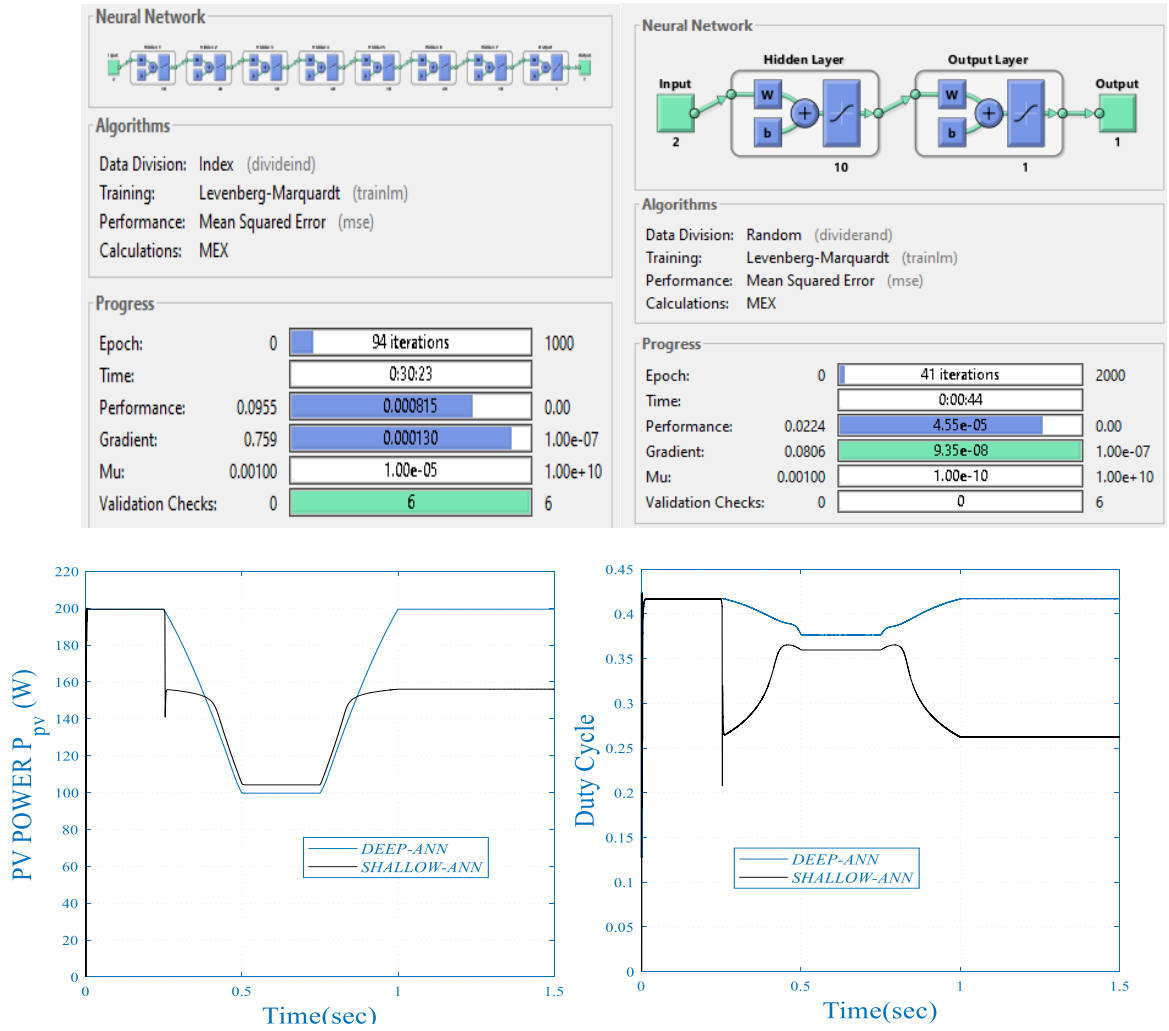


Figure (V-15): Performance Comparison of Deep and Shallow Neural Network-Based MPPT Under (PSC)

V.6.3. DNN-MPPT Algorithm with DC load under Partial Shading Condition

This section describes the implementation of a Deep Neural Network (DNN)-based MPPT algorithm on a PV array composed of five panels connected to a DC load and subjected to partial shading. The shading pattern applied is [200, 500, 500, 1000, 800] W/m², representing a non-uniform irradiance distribution. The goal is to evaluate how effectively the DNN tracks the global maximum power point (GMPP) in a scenario where multiple local maxima may exist on the power-voltage (P–V) curve (figure V-16).

The trained DNN receives PV voltage and current as inputs and predicts the optimal duty cycle for the DC-DC converter to extract maximum power. ALL training procedure (in figures 17,19 and 20) were conducted using Matlab2023.

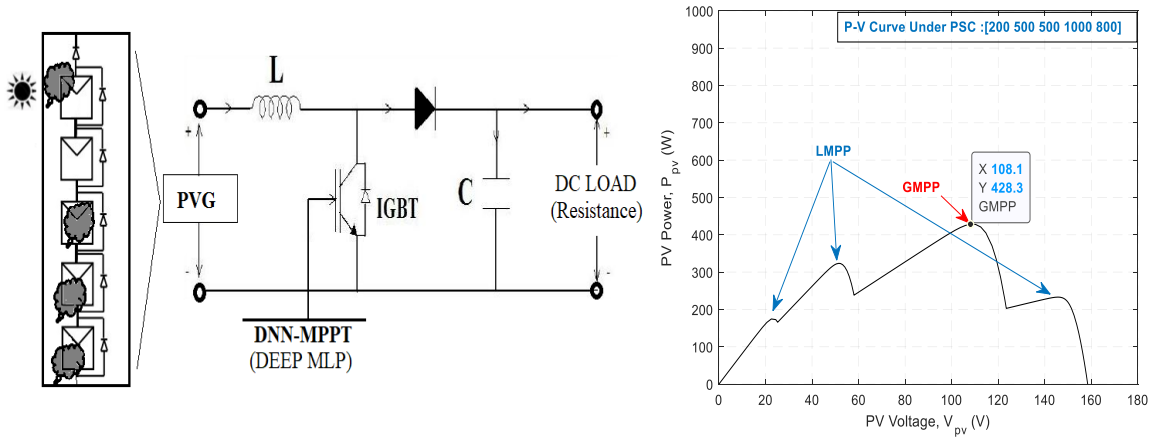


Figure (V-16): PV-DC Load and (P-V) curve under partial shading

Results demonstrate that the DNN successfully tracks the GMPP and maintains system stability despite the complexity of the shading pattern. This validates the robustness of the proposed ANN-MPPT controller in addressing partial shading challenges in PV systems.

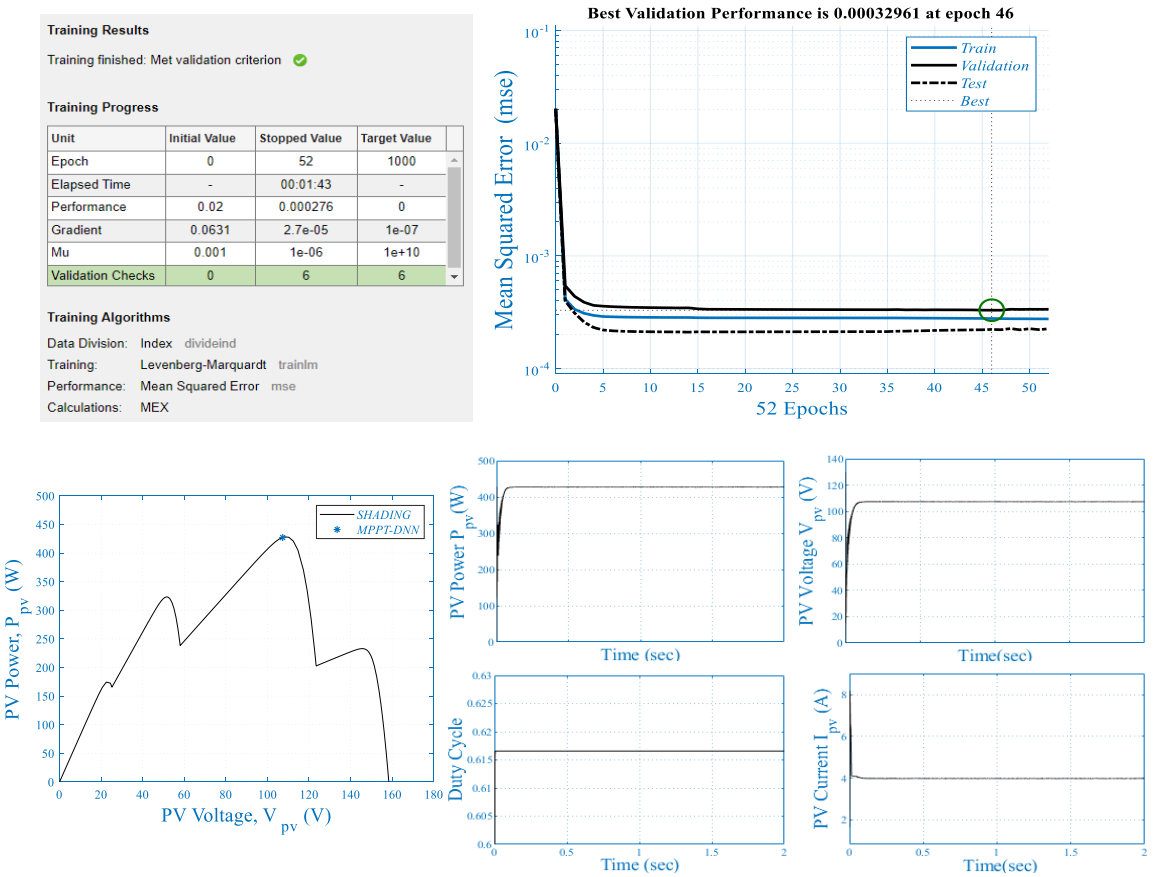


Figure (V-17): Performance Evaluation of Deep Neural Network-Based MPPT Under Partial Shading Conditions

The results (V-17) show rapid stabilization of all signals. Power reaches a consistent value around 428 W, confirming successful tracking of the global maximum power point (GMPP). PV voltage and current exhibit similar steady behavior after brief transients. The duty cycle is quickly optimized and held steady, reflecting accurate control by the ANN-MPPT. These results highlight the controller's ability to manage nonlinearities caused by shading and avoid local maxima. Overall, this confirms the ANN's real-time adaptability, stability, and superiority in complex shading environments.

V.6.4. Proposed -MPPT Algorithm with AC load (Pumping System)

This section extends the ANN-MPPT control strategy to a practical PV-powered water pumping system composed of nine panels and an induction motor (IM) driving a centrifugal pump. The configuration includes a DC-DC converter followed by a voltage source inverter controlled via Direct Torque Control (DTC). The panels are partially shaded using the distribution: one string of two panels under 500 W/m² and eight strings of two panels under 1000 W/m².

The objective is to validate the ANN controller's effectiveness in a real-world application where an AC load is involved. The DNN-MPPT is integrated into the converter stage and dynamically adjusts the duty cycle to maximize PV output. Electrical (PV power, current, voltage), mechanical (torque, rotor speed), and hydraulic (water flow and head) parameters are observed under shaded and unshaded conditions.

The simulation confirms that the ANN-MPPT successfully tracks the GMPP and maintains stable system behavior in both cases. These results prove the practicality of combining ANN-based MPPT with DTC for efficient and intelligent solar water pumping. This setup reflects a realistic renewable energy system suitable for remote water pumping applications, combining intelligent control with efficient power conversion

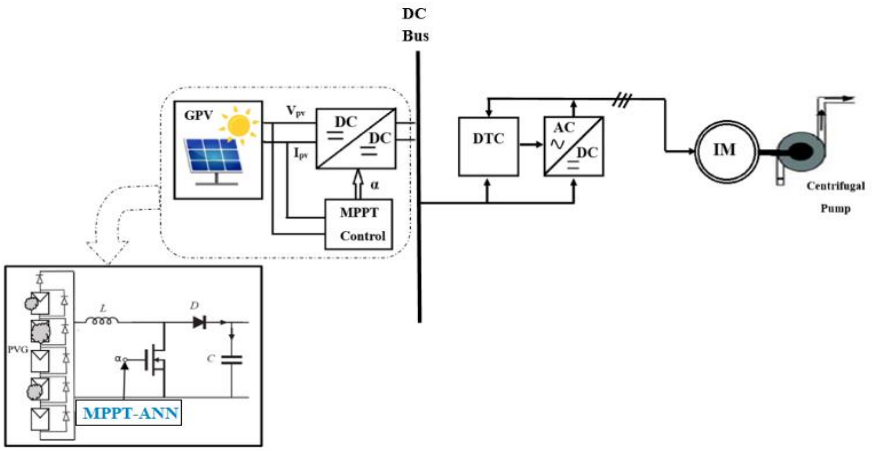
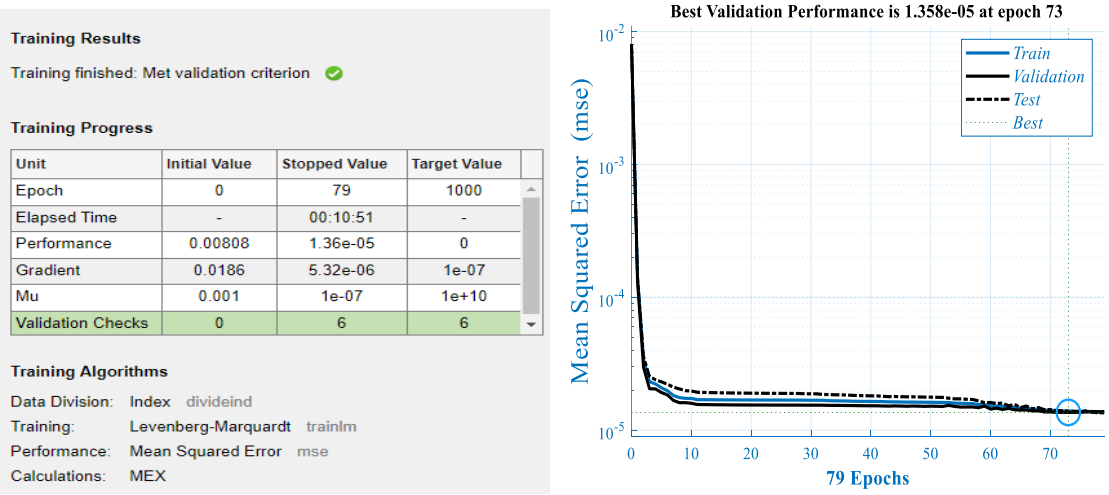


Figure (V-18): The proposed PV-Pumping system.

Figure (V.19) presents the training results of the deep neural network used for MPPT under partial shading. The left table shows training settings and outcomes: convergence was achieved after 79 epochs, with a very low final MSE of 1.36×10^{-5}. The Levenberg-Marquardt algorithm was used for optimization, known for its fast convergence. The MSE plot on the right confirms consistent error reduction across training, validation, and test datasets. The curves are closely aligned, indicating no overfitting and excellent generalization. The early stopping criterion was met after 6 checks, ensuring efficiency and stability. This proves the ANN was successfully trained to predict optimal MPPT actions across a wide range of irradiance conditions, particularly under non-uniform shading.



Training Results

Training finished: Met validation criterion

Training Progress

Unit	Initial Value	Stopped Value	Target Value
Epoch	0	79	1000
Elapsed Time	-	00:10:51	-
Performance	0.00808	1.36e-05	0
Gradient	0.0186	5.32e-06	1e-07
Mu	0.001	1e-07	1e+10
Validation Checks	0	6	6

Training Algorithms

Data Division: Index dividend
Training: Levenberg-Marquardt trainlm
Performance: Mean Squared Error mse
Calculations: MEX

Figure (V-19): Training Performance of Deep Neural Network for MPPT Under Partial Shading

The figure (V-20) shows 12 output signals from the system operating under ideal irradiance conditions (without shading). Electrical responses like PV power, voltage, and current are stable and reach their targets quickly. The rotor speed and torque of the motor converge smoothly, ensuring consistent mechanical behavior. Water flow and height remain steady, confirming reliable pump operation.

The duty cycle remains constant, validating the stability of the MPPT control. The flux and current waveforms indicate accurate DTC operation, while the flux trajectory is nearly circular, confirming proper flux vector control. Altogether, the system exhibits high efficiency, robustness, and balance in ideal solar conditions.

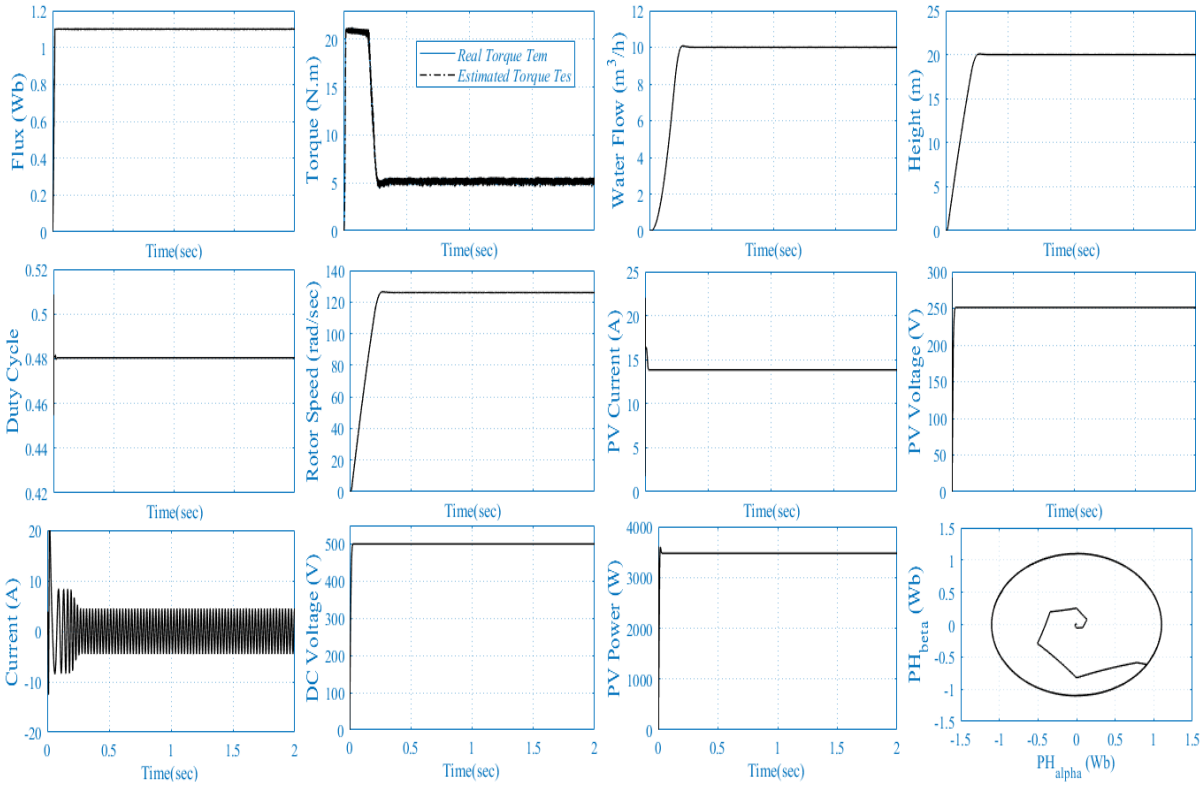


Figure (V-20): System Performance under MPPT Control Without Shading.

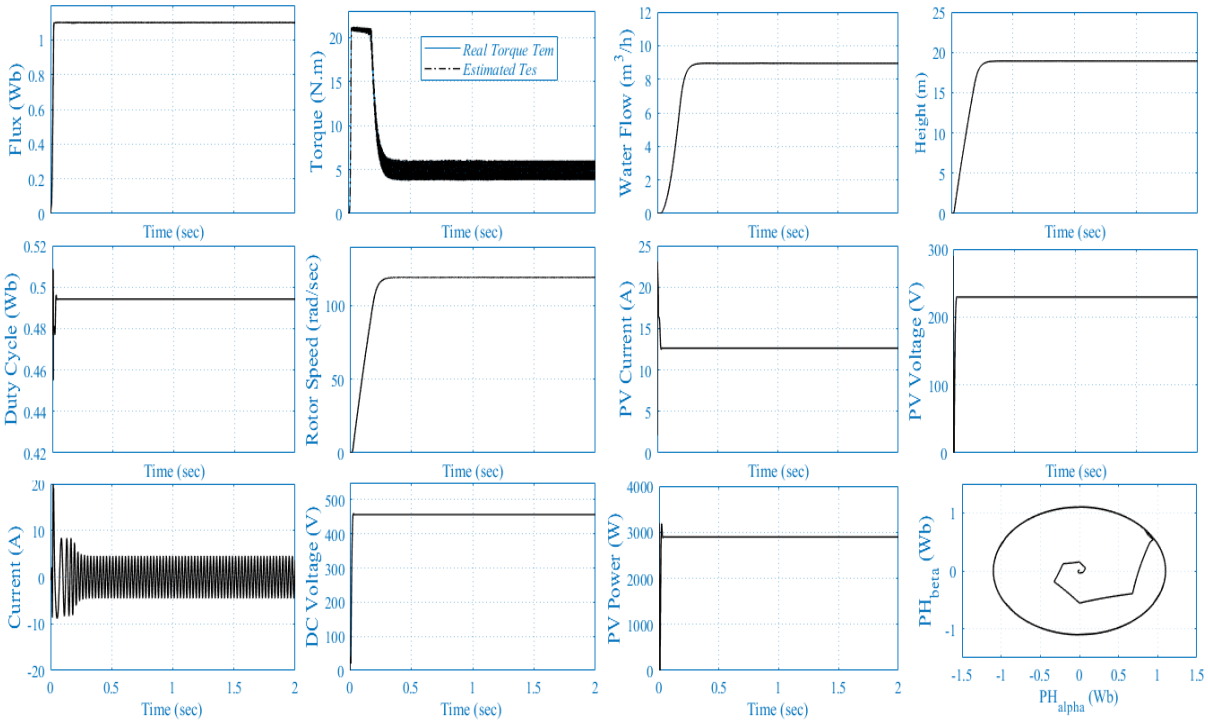


Figure (V.21): System Performance under MPPT Control with Partial Shading.

Under partial shading, this 12-subplot figure shows the system's response when part of the PV array receives lower irradiance. The ANN-MPPT still tracks the global MPP effectively, although total power and motor torque are slightly reduced compared to the ideal case. Rotor speed, water flow, and output head remain stable, confirming the system's ability to adapt.

The current and voltage waveforms indicate proper DTC and MPPT coordination. The flux trajectory remains circular and stable, indicating precise control despite shading. This result proves the ANN-MPPT controller's robustness and effectiveness in dynamically changing irradiance environments, ensuring system reliability and energy efficiency even under sub-optimal conditions. To improve system stability and performance during low irradiance periods, a water storage tank or battery energy storage is recommended. Alternatively, increasing the PV array capacity can enhance power reliability.

V.7 Conclusion:

This chapter focused on developing and evaluating a Deep Neural Network (DNN)-based MPPT strategy for photovoltaic (PV) systems, tested under different conditions and connected to both DC and AC loads. The implementation was entirely simulation-based using MATLAB/Simulink and involved real-time training data derived from PV models.

The first part involved applying the DNN to a single PV panel under dynamic irradiance. The results confirmed the deep model's ability to quickly adapt to irradiance variation and maintain power extraction with minimal oscillation. In the second part, a five-panel PV array under partial shading was tested. The DNN successfully tracked the global maximum power point (GMPP), even with multiple local maxima caused by non-uniform irradiance. In the final simulation, the DNN-MPPT was integrated into a complete PV pumping system, where energy from nine panels was used to drive an asynchronous motor via a DTC-based inverter. The system showed robust electrical, mechanical, and hydraulic performance under both ideal and shaded conditions.

Overall, the chapter confirms the DNN's ability to manage nonlinearities, respond dynamically, and maximize energy efficiency. The results highlight the value of deep learning in advancing intelligent, real-world renewable energy systems.

General Conclusion:

This thesis has presented the modeling, control, and intelligent optimization of a photovoltaic (PV) water pumping system powered by an asynchronous motor. The work focused on combining renewable energy generation with advanced control and artificial intelligence techniques to enhance performance and system reliability.

The study began with the modeling of PV systems, including the simulation of PV cell behavior under varying irradiance conditions. This foundational work enabled accurate representation of real-world solar inputs in the simulation environment. In the second chapter, the research addressed power conversion stages, particularly the Boost converter. MPPT strategies were introduced to ensure optimal energy extraction from the solar array.

The third chapter focused on the mathematical modeling of the asynchronous (induction) motor using the $d-q$ reference frame, highlighting the electromechanical dynamics of the motor when driven by a two-level VSI with PWM control.

The fourth chapter introduced Direct Torque Control (DTC) as a high-performance alternative to traditional control methods. DTC enabled fast and precise control of flux and torque without relying on PWM modulation, making it ideal for PV-driven water pumping applications.

In the final chapter, the core innovation of this work was presented: a comparative study between Shallow Neural Networks (SNN) and Deep Neural Networks (DNN) applied to MPPT control. These techniques were tested under DC load conditions to evaluate their initial performance, and then extended to an AC load scenario involving a water pumping system. Simulation results clearly demonstrated that the DNN-based MPPT provided better tracking accuracy, faster convergence to the Global Maximum Power Point (GMPP)**,** and more stable motor behavior, especially under partial shading conditions.

In conclusion, the integration of deep learning-based MPPT with DTC control in PV pumping systems significantly enhances energy efficiency and system performance. This approach offers a reliable and intelligent solution for renewable energy applications, particularly in remote or off-grid environments where adaptability and autonomy are essential.

Parameter	Value
Open circuit voltage V_{oc}	32.9 V
Short-circuit current I_{sc}	8.21 A
MPP voltage V_{mpp}	27 V
Maximum power P_{max}	200 W
Parallel resistance R_p	951.9319 Ω
Series resistance R_s	0.2172 Ω
Number of cells in series per module	54
Number of modules in series	15

Parameter	Value
Nominal power	3.5 kW
Nominal torque	10 N·m
Nominal flux	1.1 Wb
Frequency	50 Hz
Stator resistance	4.85 Ω
Rotor resistance	3.805 Ω
Stator inductance	0.274 H
Rotor inductance	0.274 H
Mutual inductance (M_{sr})	0.258 H
Moment of inertia	0.031 Kg·m²
Coefficient of friction	0.001131 IS
Number of pole pairs	2

REFERENCES

General Introduction:

[1] **Ember Energy** - *Solar power sees 29% increase in 2024, marking new record* - TechXplore, April 2025.

[2] **Chandel, S. S., Naik, M. N. & Chandel, R -** *Review of solar photovoltaic water pumping system technology for irrigation and community drinking water supplies* - Renewable and Sustainable Energy Reviews, Elsevier, 2015.

Chapitre I : Overview of PV systems

[1] **F. Chekired** – *étude et implémentation d'une commande mppt neuro-floue sur FPGA* – National Polytechnic School, Algiers, Algeria – 2008.

[2] – *Principe de la cellule photovoltaïque* – http://tepeenergiephotovoltaique.e-monsite.com/pages/la-cellule-photovoltaique/principe-de-la-cellule-photovoltaique.html

[3] **M. Blhadj** – *Modélisation d'un système de captage photovoltaïque autonome* – University Center of Bechar – 2007–2008.

[4] **M.L. Louazane** – *Étude technico-économique d'un système de pompage photovoltaïque sur le site de Ouargla* – University El Hadj Lakhdar, Batna – 2008.

[5] **S.M. Ait-Cheikh** – *Étude, investigation et conception d'algorithmes de commande appliqués aux systèmes photovoltaïques* – National Polytechnic School, Algiers, Algeria – 2007.

[6**] S. Issaadi** – *Commande d'une poursuite du point de puissance maximum (MPPT) par les réseaux de neurones* – National Polytechnic School, Algiers, Algeria – 2006.

[7] **M. Adouane** – *Étude et conception d'une stratégie de commande d'un onduleur connecté au réseau électrique* – National Polytechnic School, Algiers, Algeria – 2008.

[8] **Aghaei M., Nedaei A., Eskandari A., & Milimonfared J.** – *Introductory Chapter: Solar Photovoltaic Energy* – IntechOpen – 2022.

[9] **R. Mahto & R. John** – *Modeling of Photovoltaic Module* – IntechOpen – 2021.

[10] **International Electrotechnical Commission** – *IEC 60364 – Low-voltage electrical installations* – Geneva, Switzerland – 2020.

[11] **Housseini M., Boukheit N., & Benchabane A**. – *Performance analysis of a hybrid PV–wind–diesel system with battery storage in the Saharan region of Algeria* – Renewable Energy – 2021.

[12] **Chowdhury S., Rahman K. S., Chowdhury S. P., & Crossley P**. – *Reliability analysis of grid-connected wind energy systems* – IEEE Transactions on Power Systems – 2010.

[13] **International Energy Agency (IEA)** – *World Energy Outlook 2023* – Paris, France – 2023.

Chapter II : DC-DC Converter.

[13] **DRIDI Toufik, BENBOUABDELLAH Oumsaad** – *Commande par intelligence artificielle d'un générateur solaire photovoltaïque* – Master thesis, 2016.
[14] **K. Kassmi, M. Hamdaoui** – *Conception et modélisation d'un système photovoltaïque adapté par une commande MPPT analogique* – Revue des Énergies Renouvelables, Vol. 10, No. 4, pp. 451–462, Olivier, 2007.
[15] **C. Jena, A. Das, C. K. Panigraphi, M. Basu** – *Modelling and simulation of photovoltaic module with buck-boost converter* – International Journal of Advanced Engineering and Nano Technology (IJAENT), Vol. 01, Issue 3, pp. 18–21, 2014.
[16] **S. Sumath, L. A. Kumar, P. Surekha** – *Solar PV and Wind Energy Conversion Systems: An Introduction to Theory, Modeling with MATLAB/Simulink, and the Role of Soft Computing Techniques* – 2015.
[17] **S. Sholapur, K. R. Mohan, T. R. Narsimhegowda** – *Boost converter topology for PV system with Perturb and Observe MPPT algorithm* – IOSR Journal of Electrical and Electronics Engineering (IOSR-JEEE), e-ISSN: 2278-1676, p-ISSN: 2320-3331, Vol. 9, Issue 4, pp. 50–56, 2014. doi:10.9790/1676-09425056

Chapter III: Modeling of Induction machine

[18] **M. Rivoire, J. L. Ferrier** – *Commande par calculateur, identification* – Eyrolles, Paris, 1997.
[19] J. Lesenne, F. Notelet, G. Séguier – *Introduction à l'électrotechnique approfondie* – Technique et Documentation, Paris, 1981.
[20] M**. Ibrahim Messai, M. Mokhtar Redouan**i – *Contrôle Direct du Couple d'une Machine Asynchrone* – University of El Oued, Algeria, 2013.
[21] **Walid Bendemmagh** – *Commande de la machine asynchrone par la cascade hypo synchrone à base des logiciels s'implorer et Matlab* – University of Sétif 1, Faculty of Technology, Algeria, 2013.
[22] **Radouane Achouri, Mohamed Hidouche** – *Commande vectorielle de la machine asynchrone* – ENP, Algiers, 2007.
[23] **R. Abdessemed, M. Kadjoudj** – *Modélisation des machines électriques* – University of Batna Press, Algeria, 2011.

[24] **Malika Benaissa** – *Minimisation des pulsations du couple dans une commande directe du couple DTC d'une machine asynchrone* – University of Batna, Algeria, [year not specified].
[25] **V. I. Utkin, J. Guldner, J. Shi** – *Sliding Mode Control in Electro-Mechanical Systems* – CRC Press, Taylor & Francis Group, New York, 2009.
[26] **A. Benbrahim** – *Commande prédictive généralisée d'une machine synchrone à aimants permanents* – University of Batna, Algeria, 2009.
[27] **Claude Chevassu** – *Machines électriques* – [Place not specified], July 20, 2012.
[28] **Hanene Tamrabet** – *Robustesse d'un contrôle vectoriel de structure minimale d'une machine asynchrone* – Magister Thesis, University of Batna, Algeria, 2006.
[29] **Abdesselem Chikhi** – *Commande Directe du Couple du Moteur Asynchrone – Apport de la Logique Floue* – University of Batna, Algeria, 2008.

Chapitre IV: Direct torque control of IM

[30] **Messaoud Benamor** – *Commande par DTC de la machine à induction sans capteur de vitesse : utilisation du filtre de Kalman pour l'estimation de la vitesse* – University of Batna, Algeria, 2012.
[31] **M. Abd Elkebir, N. Merzoug** – *Contrôle direct de couple d'une machine à induction* – Engineer Thesis, University of M'Sila, Algeria, 2005.
[32] **K. Hoang** – *Comparison of Field-Oriented Control and Direct Torque Control* – IEEE, USA, 1999.
[33] **L. Cristian, I. Boldea, F. Blaabjerg** – *A Modified Direct Torque Control for Induction Motor Sensorless Drive* – IEEE Transactions on Industrial Applications, vol. 36, pp. 122–130, USA, Jan/Feb 2000.
[34] **A. Rahal, M. F. Edjiri** – *Contrôle direct du couple de la machine asynchrone* – Engineer Thesis, University of M'Sila, Algeria, 2004.
[35] **T. Lameche** – *Développement et Implémentation par Logique Floue d'une Commande DTC d'un Moteur à Induction Alimenté par un Onduleur de Tension PWM* – Magister Thesis, University of Sétif, Algeria, 2003.
[36] **A. Gallego, F. Fele, E. Camacho, L. Yebra** – *Observer-Based Model Predictive Control of a Parabolic-Trough Field* – Solar Energy, vol. 97, pp. 426–435, 2013.
[37] **A. Gallego, E. Camacho** – *Estimation of Effective Solar Irradiation Using an Unscented Kalman Filter in a Parabolic-Trough Field* – Solar Energy, vol. 86, no. 12, pp. 3512–3518, 2012.
[38] **C. Djamila, M. Yahia** – *Direct Torque Control Strategies of Induction Machine* – [Place not specified], 2021.

Chapter V: PV pumping system- based on MPPT-Deep Learning

[39] M**. A. Chaouch, et al.** – *Artificial Neural Network-Based MPPT Control for PV Systems* – Renewable Energy, vol. 152, pp. 1170–1180, 2020.
[40] **S. Haykin** – *Neural Networks and Learning Machines*, 3rd Edition – Pearson, USA, 2009.
[41] D. E. Rumelhart, G. E. Hinton, R. J. Williams – *Learning Representations by Back-Propagating Errors* – Nature, vol. 323, pp. 533–536, 1986.
[42] **K. Hornik** – *Approximation Capabilities of Multilayer Feedforward Networks* – Neural Networks, vol. 4, no. 2, pp. 251–257, 1991.
[43] **Y. LeCun, Y. Bengio, G. Hinton** – *Deep Learning* – Nature, vol. 521, no. 7553, pp. 436–444, 2015.
[44] **I. Goodfellow, Y. Bengio, A. Courville** – *Deep Learning* – MIT Press, USA, 2016.
[45] **N. Srivastava, et al.** – *Dropout: A Simple Way to Prevent Neural Networks from Overfitting* – Journal of Machine Learning Research (JMLR), 2014.
[46] **R. Ben Ali, W. Rekik, L. Krichen** – *ANN-Based MPPT for Photovoltaic Pumping System Under Varying Solar Radiation* – Solar Energy, vol. 166, pp. 190–199, 2018.